NASA TECHNICAL MEMORANDUM

NASA TM X-3244

NASA TM X-3244

DETAILED TRANSONIC FLOW FIELD MEASUREMENTS ABOUT A SUPERCRITICAL AIRFOIL SECTION

Francis X. Hurley, Frank W. Spaid, Frederick W. Roos, Louis S. Stivers, Jr., and Angelo Bandettini

Ames Research Center
Moffett Field, Calif. 94035

NATIONAL AERONAUTICS AND SPACE ADMINISTRATION • WASHINGTON, D. C. • JULY 1975

1. Report No.	2. Government Accession No.	3. Recipient's Catalog No.
NASA TM X-3244		

4. Title and Subtitle	5. Report Date
DETAILED TRANSONIC FLOW FIELD MEASUREMENTS ABOUT A SUPERCRITICAL AIRFOIL SECTION	July 1975
	6. Performing Organization Code

7. Author(s)	8. Performing Organization Report No.
Francis X. Hurley, Frank W. Spaid, Frederick W. Roos, Louis S. Stivers, Jr., and Angelo Bandettini	A-5869
	10. Work Unit No. 505-06-31

9. Performing Organization Name and Address	11. Contract or Grant No.
McDonnell Douglas Research Laboratories McDonnell Douglas Corporation St. Louis, Missouri 63166, and Ames Research Center Moffett Field, California 94035	

12. Sponsoring Agency Name and Address	13. Type of Report and Period Covered
National Aeronautics and Space Administration Washington, D. C. 20546	Technical Memorandum
	14. Sponsoring Agency Code

15. Supplementary Notes

16. Abstract

Detailed measurements in the transonic flow field about a Whitcomb-type supercritical airfoil profile are presented. In addition to the usual surface pressure distributions and wake surveys, schlieren photographs were taken and velocity vector profiles were determined in the upper surface boundary layer and in the near wake. Spanwise variations in the measured pressures were also determined.

The data are analyzed with the aid of an inviscid transonic finite-difference computer program as well as boundary layer modeling and calculation schemes; these data analyses aid in the understanding of transonic viscous-inviscid interactions. Recommendations are made regarding future tests and extensions of the present measurements.

Comprehensive dynamic measurements made during the course of this program are reported separately.

17. Key Words (Suggested by Author(s))	18. Distribution Statement
Supercritical airfoil section, Transonic profile flowfield, Pressure distributions, Boundary-layer profiles, Boundary-layer properties, Near-wake profiles, Spanwise pressure deviations	Unclassified – Unlimited STAR Category – 02

19. Security Classif. (of this report)	20. Security Classif. (of this page)	21. No. of Pages	22. Price*
Unclassified	Unclassified	64	$4.25

*For sale by the National Technical Information Service, Springfield, Virginia 22151

NOTATION

a function of M_e, γ, and r in van Driest transformation, Eq. (3)

C_f skin friction coefficient, $\frac{\tau}{q_\infty}$

C_f^* skin friction coefficient computed from transformed speed profile, u^*

C_p pressure coefficient, $\frac{p - p_\infty}{q_\infty}$

c airfoil chord

c_d airfoil section drag coefficient, $\int_{\text{wake}} c_d' \, d(z/c)$

c_d' airfoil section point drag coefficient, $2\left(\frac{p_{t_r}}{p_{t_\infty}}\right)^{\gamma-1/\gamma}\left(\frac{p_r}{p_\infty}\right)^{1/\gamma}\left[\frac{1-(p_r/p_{t_r})^{\gamma-1/\gamma}}{1-(p_\infty/p_{t_\infty})^{\gamma-1/\gamma}}\right]^{1/2}$

$$\times\left[1-\left(\frac{1-(p_\infty/p_{t_r})^{\gamma-1/\gamma}}{1-(p_\infty/p_{t_\infty})^{\gamma-1/\gamma}}\right)^{1/2}\right]$$

---

c_l airfoil section lift coefficient, $\frac{L}{q_\infty c}$

d probe tip thickness

H boundary-layer shape factor, $\frac{\delta^*}{\theta}$

L airfoil lift per unit span

M free-stream Mach number

p static pressure

p_t total pressure

q dynamic pressure, $\frac{1}{2}\rho u^2$

Re_c Reynolds number based on free-stream conditions and airfoil chord

R_{le} airfoil leading edge radius

r recovery factor

T_{STAG} stagnation temperature

u speed

u^* speed transformed by Van Driest transformation, Eqs. (2) and (3) of text

u_τ shear velocity, $\sqrt{\tau_w/\rho_w}$

w empirical wake function, Eq. (5)

x coordinate measured parallel to free-stream direction

y spanwise coordinate

z coordinate normal to x-y plane

α angle of attack, corrected for the effects of the wind tunnel walls

α_{geom} geometric angle of attack, uncorrected

γ specific heat ratio

δ boundary layer thickness

δ^* boundary layer displacement thickness, $\int_0^\delta \left(1-\frac{\rho u}{\rho_e u_e}\right)dz$

ϵ angular correction applied to triple probe data (fig. 27)

θ boundary layer momentum thickness, $\int_0^\delta \frac{\rho u}{\rho_e u_e}\left(1-\frac{u}{u_e}\right)dz$

ν kinematic viscosity

Π wake coefficient for transformed boundary layer profile, Eq. (4)

π 3.142

ρ density

τ shear stress

Subscripts

c based on airfoil chord

e conditions at edge of boundary layer

r	condition at rake
te	trailing edge
w	conditions at the airfoil surface
∞	free-stream conditions

DETAILED TRANSONIC FLOW FIELD MEASUREMENTS ABOUT A SUPERCRITICAL AIRFOIL SECTION*

Francis X. Hurley, Frank W. Spaid, and Frederick W. Roos
McDonnell Douglas Research Laboratories
and
Louis S. Stivers, Jr., and Angelo Bandettini
Ames Research Center

SUMMARY

Detailed measurements in the transonic flow field about a Whitcomb type supercritical airfoil profile are presented. In addition to the usual surface pressure distributions and wake surveys, schlieren photographs were taken and velocity vector profiles were determined in the upper surface boundary layer and in the near wake. Spanwise variations in the measured pressures were also determined.

The data are analyzed with the aid of an inviscid transonic finite-difference computer program as well as boundary layer modeling and calculation schemes; these data analyses aid in the understanding of transonic viscous-inviscid interactions. Recommendations are made regarding future tests and extensions of the present measurements.

Comprehensive dynamic measurements made during the course of this program are reported separately.

INTRODUCTION

The Mach number, lift-coefficient flight envelopes of modern jet aircraft operating in the high subsonic and transonic speed regimes are limited by compressibility drag rise and by the buffeting phenomenon. Therefore, airfoil section designs which alleviate or delay the onset of drag rise and buffeting can contribute to higher maximum speeds (transport application) or better lift performance (fighter application).

The Whitcomb NASA supercritical airfoil section introduced in 1966 demonstrated an increase in drag-rise Mach number compared with conventional airfoils (ref. 1). Since that time, NASA has explored various profile refinements (e.g., refs. 2 and 3) and has embarked on several full-scale flight test programs in cooperation with the Department of Defense (e.g., ref. 4). A review of supercritical aerodynamics is given in reference 5.

*This research was conducted in part under the McDonnell Douglas Independent Research and Development Program.

Various related research projects aimed at specific applications of the supercritical profile have also been conducted within industry. Efforts by Yoshihara and his co-workers at General Dynamics on powered supercritical profiles are reported in reference 6. Within McDonnell Douglas Corporation (MDC), both McDonnell Aircraft Company (MCAIR) and Douglas Aircraft Company (DAC) have done research on low-moment supercritical profiles (ref. 7) and on conventional cambered "rooftop" and "peaky" profiles as well as aft cambered supercritical profiles (ref. 8). Typical computer analysis (inviscid) methods are summarized in references 9–11. The reports noted here are representative; the transonic airfoil section literature is voluminous and growing.

The above references mainly describe performance measurements. It was reasoned that continued airfoil design efforts would benefit from a more detailed experimental study of the flow field of a supercritical airfoil throughout a range of Mach numbers extending from below to well beyond that for drag divergence. Such a study should lead to design optimizations to forestall buffeting and drag rise, or to a definition of the limits to which these can be forestalled. This is also the philosophy behind the data presented in reference 12.

McDonnell Douglas Research Laboratories (MDRL) performed flow field experiments in a small MDC facility using an airfoil designated DSMA (Douglas Santa Monica Airfoil) 523, which is essentially the original NASA Whitcomb integral (unslotted) supercritical profile (ref. 1). In addition to the standard surface pressure (lift) distributions and wake (drag) surveys, the data from those tests included schlieren photographs, near-wake surveys, and hot wire anemometer wake flow fluctuation records. The measurements, presented in reference 13, correlated the approach and the occurrence of the abrupt transonic drag rise with large shock systems and with trailing edge separations on both the upper and lower surfaces (depending on the value of lift coefficient) and with single point wake fluctuation energy.

Analysis of the data of reference 13, however, has indicated the need for a larger test facility and more sophisticated equipment in order to acquire sufficiently detailed data. The detail required would be comparable to or exceed that discussed in references 14 and 15 for configurations other than supercritical airfoil profiles. Therefore, MDRL conducted a series of tests on the DSMA 523 profile in the NASA Ames Two- by Two-Foot Transonic Wind Tunnel, utilizing supplementary instrumentation. The results of these tests are the subject of this report.

The experiments described herein were engineered primarily to provide two types of supercritical profile data that are not yet available in the open literature (especially for conditions through buffet onset and drag divergence). These data are: (1) velocity vector profiles in the boundary layer and in the near-wake, together with more conventional measurements; and (2) dynamic data, which are being reported separately, that include surface pressure fluctuations, wake flow unsteadiness, and model vibrations.

Some types of measurements were made at several spanwise stations in order to allow at least a partial evaluation of the severity of three-dimensional effects. The oil-flow studies of reference 16 indicated that essentially two-dimensional results might be difficult to achieve.

APPARATUS AND TEST PROCEDURE

Wind Tunnel

Figure 1 presents the layout and principal parameters of the NASA Ames Research Center Two- by Two-Foot Transonic Wind Tunnel, a variable-speed, continuous-flow, ventilated-wall, variable pressure facility. This facility was re-engineered by NASA for occasional two-dimensional research testing by adding motorized, rotating, thick-glass, model-supporting side windows mounted in unventilated, plane side walls. A unit Reynolds number of 26.25×10^6 per meter (8.0×10^6 per foot) generally can be maintained for long runs (15–30 min) while a high subsonic Mach number is held to within about ±0.002. An 82-tube drag rake (programmed to provide total pressure readings every 1.3 mm (0.050 in.) and static pressure readings every 25.4 mm (1.0 in.) across the wake of the model) and a spark schlieren camera are available. The Beckmann data collection system provides a paper tape output for data reduction of the fundamental parameters.

Probe

A probe rig provided by MDRL for mating with the original tunnel sting mount resulted in fully three-dimensional probe traversing capability. Vertical (normal-to-surface) motion was of high resolution – as little as 0.051 mm (0.002 in.) – between points for boundary layer traverses; both vertical and spanwise motion were remotely controlled and monitored during a run. The major elements in the actuating and tracing of the vertical motion were a geared-down dc motor with an angled drive shaft, a dove-tailed mounting block for the probe attachment, and a Wheatstone bridge. One element of the bridge was a segment of closely-wound, high-resistance wire marked off by the moving probe holder. The test section occupied by the probe rig and the airfoil model is shown in figure 2.

A photograph of the triple probe and a sketch of the tip geometry are shown in figure 3. The tip was fabricated from three pieces of 0.25 mm (0.010 in.) outside diameter stainless steel tubing, flattened and ground at the end to the dimensions indicated in the figure. The flattened ends were aligned horizontally and cemented together with epoxy. The end of the center tube was cut normal to the tip axis, and the ends of the outer tubes were cut in planes ±45° with respect to the center tube.

The present combination of test section pressure levels, small probe tip dimensions, and substantial tubing volume resulted in a time delay for stabilizing the indicated pressure. Approximately 5 sec were required to obtain an accurate reading at the lowest pitot pressure.

Data obtained from the center tube were interpreted in the manner of conventional pitot-tube data. Estimates based on a survey of the current literature indicated that the measurement inaccuracy caused by shear should be negligibly small. Errors in mean pitot pressure resulting from turbulent fluctuations could be significant, particularly in the near-wake, but no known method of correction is adequate. The proximity of the probe to the surface of the airfoil model is known to have caused errors in some of the pressure probe data; this effect is discussed later in connection with boundary layer data analysis. Probe support blockage may have influenced the flow over the airfoil during a boundary layer survey. Although insufficient data were obtained to make a

quantitative assessment of this effect (i.e., no airfoil static pressure data were taken with the probe in position), results of a similar investigation of a transonic airfoil boundary layer reported by Cook (ref. 14) suggest that this effect is probably small.

Pitot pressure measurements from the center orifice of the triple probe were reduced as boundary layer and wake data in the conventional manner. Mach number profiles were determined from the pitot pressures and the airfoil surface static pressure (measured in the absence of the probe), using the isentropic formula or the Rayleigh pitot formula. Speed, temperature, and density were then computed from perfect-gas relations, with the assumptions of constant static pressure at a given survey station, and constant stagnation temperature throughout the flow field. Near-wake speeds were computed using the assumption that the static pressure was constant and equal to the freestream value. This assumption undoubtedly is the source of significant errors in near-wake speeds computed for points close to the trailing edge.

Data from the three orifices of the triple probe were used to determine flow direction in the pitch plane. The probe was calibrated with the aid of a small free-jet facility that exhausted to atmosphere. The tip was placed in the inviscid core of the jet, and angles between the probe shaft and the jet nozzle were measured to the nearest 0.002 rad (0.1°). Figure 4 is a typical probe calibration curve presenting the flow inclination angle versus the differences between the pressures measured by the two outer tubes, normalized by the center tube pressure, for various Mach numbers. These results show that this method of data presentation is insensitive to speed, for $M \geqslant 0.8$, and that the accuracy of this technique for determining flow angularity decreases with decreasing Mach number. Additional data (not reported here) were obtained for intermediate Mach numbers between 0.2 and 0.6. Calibration curves in which the normalized pressure difference was plotted versus Mach number at constant inclination angle also were used in the data reduction process.

A comparison of flow inclination angles measured by the probe with streamline directions determined by other means revealed an apparent constant bias in the probe angles. A correction for this bias has been applied to all probe data. The method by which this correction was determined is described later in the Flow-Field Composites subsection of the RESULTS AND DISCUSSION section of this paper.

Since the static pressure and stagnation temperature of the jet were essentially constant during the calibration of the probe, the Mach and Reynolds numbers near the probe tip were varied simultaneously. Although the data obtained from calibrations of other types of flow-angularity probes suggest that the variation shown in figure 4 is primarily a Mach number effect (see ref. 17), the present calibration data do not eliminate the possibility of an independent influence of Reynolds number. Fortunately, this question is unimportant, since both the static pressure and stagnation temperature were nearly the same in the calibration as in the test. Consequently, the variation of Reynolds number with Mach number in both cases was nearly the same, as shown in figure 5.

The influence of proximity to a surface on the indicated flow inclination angle was investigated by a series of calibration runs in which a razor blade was mounted in the jet and aligned with the flow. The error was found to depend on the Mach number, the distance to the surface, and the angle between the probe tip and the flow direction. The error remained small, ±0.009 rad (±0.50°), when the distance from the surface was greater than 0.66 mm (0.026 in.). In these experiments, the point at which the flow directions could not be accurately determined as a result of a low local

Mach number was always located at a distance from the surface greater than that where the proximity effect first became significant.

The possibility of using the probe data to determine the local static pressure was investigated. It was found that the static pressure value obtained from the probe data was excessively sensitive to uncertainties in flow inclination angle.

Airfoil Model

The DSMA 523 profile, tested in this investigation, is essentially the original NASA Whitcomb integral (unslotted) supercritical profile (ref. 1) except that the rearward lower surface was modified to accommodate a finite trailing edge thickness (equal to 1 percent chord on this model) and a smoothing process has been applied to the ordinates. The profile coordinates are listed in table 1. The model was constructed of stainless steel to have a 15.24 cm (6 in.) chord and to span fully the width of the wind tunnel test section. The model was equipped with 125 static pressure orifices – 0.203 mm (0.008 in.) diameter – in order to establish chordwise as well as spanwise variations in static pressure. The locations of these orifices are shown in figure 6.

A leading-edge transition band was applied, observing the recommendations of reference 18, although initial tests were made with a transition band located at 12 percent chord on both the upper and lower surfaces (see table 2). The leading-edge location was chosen in an attempt to ensure that the boundary layer would always be turbulent upstream of the shock wave (or initial separation point), and thus avoid anomalies in the measured data which arise from interactions between the shock wave and a laminar boundary layer. It is realized, however, that transition near the leading edge, for the Reynolds numbers of the present tests, results in somewhat thicker boundary layers and possibly in more severe separation over the rearward portion of the upper surface of the model (see ref. 19) than would be typical of flight Reynolds numbers.

RESULTS AND DISCUSSION

Data representative of the various types of measurements performed in this test series are presented herein. The choices of runs and plots for presentation in this report were made according to the criteria that significant new information should appear in each figure and that repetition should be avoided; however, the senior authors will supply the unpublished data upon request.

Overall Flow Field

Figure 7 shows the variation of chordwise pressure distribution with lift coefficient and Mach number. The lift contribution of the rearward camber is conserved over a wide range of conditions, including the development of lower surface suction at low c_l. Increasing Mach number delays the upper surface recompression to more rearward stations.

The corresponding schlieren photographs are presented in figure 8. It is seen that the vertical extent (as well as the strength) of the shock waves is substantial at a Mach number of 0.86, and that

shock compression may appear on the lower surface (as well as the upper surface) at positive lift ($c_l = 0.30$, $M = 0.82$). Double shock compressions appear at $c_l = 0.51$, $M = 0.82$. The wake is visibly broadened at high speeds ($M = 0.86$). A portion of the lower surface concavity appears to be separated at all conditions shown, but this may be a condition only at the tunnel walls, since extensive separation is not indicated by the pressure distributions of figure 7.

A summary of the lift coefficients, resolved from the integration of the pressure distributions for a variety of parameters, is given in table 2.

The development of the wake (drag) profiles with increasing Mach number is shown in figure 9. There is some deepening, but the major effect is one of wake broadening, skewed to the upper surface side, indicating increased upper surface shock losses.

The transonic drag rise behavior of the airfoil, obtained by integrating wake profiles measured at various stations under a variety of flow conditions and parameters, is shown in figure 10. The shaded curve, which corresponds to c_l values from 0.3 to 0.7, shows a roughly constant value of c_d at the lower Mach numbers, with a rapid rise beginning in the vicinity of a Mach number of 0.81.

The drag level in the lower Mach number range is higher than would be computed for the airfoil at subsonic conditions at the test Reynolds number, with transition fixed at the leading edge. Upper-surface shocks, which already exist for a Mach number of 0.75, relatively thick boundary layers, and a possible separated region on the aft portion of the lower surface, are believed to contribute to this drag level. A study of the schlieren photographs, comparisons between experimental and computed pressure distributions (an example of which will be presented later), and more recent unpublished data indicate that a separation bubble may have existed in the lower surface concavity during most of the present series of tests. Table 3 summarizes the plotted points and other (redundant) data.

Triple Probe Vector Profiles

Velocity vector profiles at $x/c = 0.95$, 1.00, and 1.05 at $M = 0.83$ are presented in figure 11.

The origins of the z/c axes for the near-wake profiles are aligned vertically with the upper corner of the trailing edge. The position of the tail of each arrow on the ordinate corresponds to the measurement location. The arrow is drawn in the indicated flow direction, with a length proportional to the speed. As a result, a curve connecting the tips of the arrows does not quite correspond to a conventional speed profile. Data points indicated by circular symbols rather than arrows correspond to local Mach numbers which were too low to allow the flow angle to be determined. These points are projected from the vertical axis along lines approximately parallel to the nearest measured flow direction. Regions of reverse flow may exist where the circular symbols are shown at zero speed.

The flow is attached at $x/c = 0.95$, and a small amount of separation is indicated at the trailing edge. The near-wake is highly asymmetric as a result of the thick boundary layer and shock losses on the upper surface. The flow inclination angle within the boundary layer for $x/c = 0.95$ and 1.00 does not vary appreciably with z/c, but the near-wake profile shows a substantial vertical component of velocity for small values of z/c less than zero. Apparently, the lower surface

streamlines incline upward about the thick trailing edge and its associated dead-water region, thus continuing the expansion that is seen in the last 5 percent chord of the pressure distributions.

The influence of free-stream Mach number on the flow near the trailing edge is illustrated by figures 12 and 13. (A portion of the scatter near $z/c = 0$ can be ascribed to small variations in free-stream Mach number during a traverse.) The extent of trailing-edge separation is seen to increase rapidly with Mach number at $M > 0.83$. At $M = 0.86$, the flow direction varies significantly through the shear layer, showing a substantial vertical component as the edge of the reverse-flow region is approached.

Figure 14 presents near-wake profiles for $M = 0.83$ and for $x/c = 1.05$ to 1.50, plotted with a different vertical scale from that used in the preceding figures. The gradients in speed and inclination angle are seen to be smoothed quite rapidly in this x/c range as x/c is increased, so that the flow is nearly parallel at $x/c = 1.5$.

Near-wake data representative of the above ($c_l = 0.54$, $M = 0.83$, $x/c = 1.05$) in a scalar format, i.e., speed ratio magnitude and direction, are plotted in figure 15. It is seen that the maximum gradient in flow angularity occurs in the region where the speed is the lowest, as is the case for example at a free stagnation (wake closure) point. Such a point must exist, farther upstream, near the finite-thickness trailing edge.

Boundary Layer and Near-Wake Profile Analysis

Integrals required for determination of boundary layer and near-wake displacement and momentum thicknesses were evaluated numerically, using a version of Simpson's rule which was modified to allow a variable interval of integration. The point measured nearest the surface was eliminated from the integrands (but has been included in most figures). This is equivalent to omitting data for which $zu_\tau/\nu_w < 40$, where u_τ is the shear velocity $\sqrt{\tau_w/\rho_w}$, τ is the shear stress, ρ is the density, ν is the kinematic viscosity, and the subscript w refers to conditions at the surface. This criterion is supported by data correlations presented later, and is not greatly different from Coles' recommendation that a universal profile be used to represent integrands when $zu_\tau/\nu < 50$ for incompressible boundary layer data (ref. 20).

Skin friction coefficients were computed from speed profiles corresponding to attached flow by performing least-squares fits of the inner portions of the profiles to the law-of-the-wall.

$$\frac{u}{u_\tau} = \frac{1}{0.41} \ln\left(\frac{zu_\tau}{\nu_w}\right) + 5.0 \tag{1}$$

A numerical iterative method was employed, using data for which the magnitude of zu_τ/ν_w is between 50 and 300. The extent of the logarithmic region of each speed profile was determined from inspection of preliminary reduced data, and the upper limit of the fitted region was decreased slightly for some of the nearly separated profiles.

Speed profiles corresponding to incompressible flow were obtained from the physical profiles by means of the van Driest transformation (ref. 21).

$$u^* = \frac{u_e}{a} \sin^{-1}\left(a \frac{u}{u_e}\right) \tag{2}$$

where

$$a = \left(\frac{r \frac{\gamma-1}{2} M_e^2}{1 + r \frac{\gamma-1}{2} M_e^2}\right)^{1/2} \tag{3}$$

The subscript e refers to edge conditions and r is the recovery factor, taken to be 0.89. The transformed profiles were fitted (by an iterative least-squares technique) to Coles' wall-wake formula (ref. 20).

$$\frac{u^*}{u_\tau} = \frac{1}{0.41} ln\left(\frac{z u_\tau}{\nu_w}\right) + 5.0 + \frac{2\Pi}{0.41} \sin^2\left(\frac{\pi z}{2\delta}\right) \tag{4}$$

where u_τ, Π, and δ were determined by the fitting process. The data points used in the law-of-the-wall fit were selected as described previously. The compressibility transformation had little effect on the law-of-the-wall region, and skin friction coefficients determined from the transformed speed profiles differed little from those obtained from the physical profiles. Convergence of the wake portion was sensitive to the choice of limits of the fitted region. These limits are indicated on the plotted data.

Table 4 contains boundary layer integral properties, skin friction coefficients, and related information. The corresponding quantities for near-wake surveys are presented in table 5.

Figure 16 compares upper surface boundary layer integral properties and skin friction coefficients measured at $M = 0.83$, $c_l = 0.54$, with calculations obtained from the (MDC) Cebeci program, reference 22. The measured pressure distribution was used in the calculation, with the assumption that transition occurred near the leading edge. The measured and calculated values of momentum thickness are in excellent agreement, indicating that leading edge transition was successfully effected in the experiment. The agreement between the measured and calculated skin friction is also acceptable. However, the calculation does not predict the speed profile accurately near the trailing edge, as illustrated by the lack of agreement between calculated and measured displacement thickness and shape factor.

Integral properties of the airfoil wake, also obtained for $M = 0.83$, $c_l = 0.54$, are presented in figure 17. The apparent variation in momentum defect may be primarily caused by variations in static pressure, which were not considered in the data reduction process. It is not possible to connect these results directly with those obtained on the airfoil, since the lower surface boundary layer profiles were not measured.

The series of upper surface speed profiles corresponding to $M = 0.83$, $c_l = 0.54$, are presented in figure 18 in law-of-the-wall coordinates. These data have been transformed by the method of van Driest.

The vertical flags on some of the data points denote the upper limit of the region used to fit the law-of-the-wall, when the maximum value of zu_τ/ν_w used in the fitted region was less than 300. The data obtained nearest the surface are seen to lie significantly above the universal curve. This behavior is interpreted as an indication of surface interference with the pitot-pressure measurement. Although significant scatter is present, a logarithmic region can be observed for each of the profiles. The profile obtained at the most forward station on the airfoil, $x/c = 0.3$, shows negligible deviation from a straight line (i.e., no wake component), a characteristic of boundary layers associated with low Reynolds numbers or favorable pressure gradients (ref. 20). Each of the other profiles shows substantial wake components.

Figure 19 presents the normalized wake components of the same profiles ($M = 0.83$, $c_l = 0.54$) that were presented in figure 18 together with Coles' empirical wake function.

$$w = 2 \sin^2 \left(\frac{\pi}{2} \frac{z}{\delta} \right) \tag{5}$$

Data points with vertical flags indicate the upper and lower limits of the region used in the fitting process. Some data scatter is present, but the overall agreement indicates that these profiles fit well into the wall-wake representation. Poor correlation of the points nearest the surface again is indicated. Large values of Π, the wake coefficient, correspond to boundary layers approaching separation. The largest values were obtained just downstream of the shock, at $x/c = 0.7$, and near the trailing edge.

Data similar to those presented in figures 18 and 19 are given in figures 20 and 21 for $M = 0.84$, $c_l = 0.58$. In this case, the profile corresponding to $x/c = 0.7$ has a relatively high value of C_f^* and a small value of Π, indicating a nearly flat-plate character. The much smaller C_f^* and larger Π at $x/c = 0.8$ indicates that the shock was located between these two stations. Data obtained at $x/c = 0.7$ for several values of freestream Mach number are presented in figures 22 and 23, which show behavior similar to that of the preceding plots.

Finally, these measured speed profiles have been compared directly with analytical predictions from the Cebeci computer program (ref. 22). The upper surface boundary layer development for the condition $M = 0.83$, $c_l = 0.54$ is presented in figure 24. The turbulent boundary layer experiences considerable thickening in both compressions, and becomes separated upon reaching the trailing edge. As previously shown in figure 7, the upper surface shock is around 64 percent chord at this condition, and the second compression occurs between the 80 percent chord station and the trailing edge. The Cebeci program predicts the experimental data reasonably well, except within and just downstream of the sharp pressure rises. For the $x/c = 0.80$ station, the fact that the Cebeci program calculations for leading-edge transition are in much better agreement with the experimental data than are the calculations for transition located at 30-percent chord indicates that transition must have occurred well forward of 30 percent chord. The inclusion of measurements from an extra run in the 90-percent chord plot indicates that data repeatability was good. In these graphs, the probe tip depth $d/c \cong 0.0006$ is shown on the vertical axis from the origin.

Measured and calculated profiles at the 70-percent chord station for Mach numbers that result in different relative shock locations are compared in figure 25. At $M = 0.80$, the shock wave is sufficiently far upstream so that the boundary layer has been rehabilitated upon reaching the

70-percent station, and the Cebeci prediction is good. At $M = 0.83$, the shock wave is only slightly upstream, and the Cebeci prediction is poor. At $M = 0.86$, the shock wave has been swept downstream of the measuring station, and the Cebeci prediction is good.

Figure 26 shows the upper and lower surface profiles at the trailing edge, measured and computed, for a Mach number of 0.60 and a c_l of 0.91. The lower surface boundary layer is an order of magnitude thinner than that of the upper surface, having undergone an extremely favorable pressure gradient in the last few percent of chord, and the Cebeci prediction is good. The opposite is true of the upper surface boundary layer, and the corresponding Cebeci prediction is poor.

Flow Field Composites

Composite sketches of flow fields in the vicinity of the trailing edge for the conditions $M = 0.83, c_l = 0.54$ and $M = 0.84, c_l = 0.58$, respectively, are shown in figures 27 and 28.

The vertical scale is doubled relative to the horizontal scale. Boundary layer and wake speed profiles have been plotted at each chordwise station. Speeds have been normalized by the freestream value, thus showing the deceleration of the flow at the boundary-layer edge as the trailing edge is approached, and illustrating the fact that speeds exterior to the boundary layer and to the near-wake are nearly equal to that of the freestream. Flow directions obtained from the triple probe data have been indicated at selected stations. Since the flow direction arrows have been drawn inside the speed profile envelopes the lengths of these arrows are not quite to scale.

Values of δ obtained from the wall-wake fitting process are indicated by the open circular symbols for each velocity profile. The displacement thickness distribution and two streamlines are also indicated. The streamlines were constructed by computing running integrals of mass flux from the boundary layer speed and density profiles, beginning at the wall. It is believed that these streamlines can be used to determine the local flow inclination with reasonable accuracy, estimated to be within ±0.03 rad (±1.5°) for the data of figure 27 for x/c between 0.8 and 0.95. A comparison of angles determined by the triple probe in this region with values of flow inclination determined from these streamlines showed a nearly constant shift of 0.0663 rad (3.8°). (This difference between the streamline angle and the uncorrected probe measurement is indicated in fig. 27.) Since the procedures for calibration and installation of the probe lead to substantially greater confidence in the measurement of increments in flow inclination between points than in the determination of absolute flow direction, the most probable cause of this shift is believed to be a constant error in the probe incidence as mounted in the tunnel. As a result of this comparison, a 0.0663 rad (3.8°) correction has been added to all of the triple probe data.

Figure 27 ($M = 0.83$) illustrates in a more graphic way some of the trends discussed earlier, including the thickened boundary layer at 70-percent chord (downstream of the shock), its subsequent recovery, and its further thickening and start of separation in the last 10 percent of the chord. Both the streamlines and the δ^* distribution are approximately parallel to the airfoil surface for $x/c < 0.9$, and the rapid increase in δ^* near the trailing edge causes an effective reduction in aft camber.

The wake is convected downward and spreads rapidly with increasing downstream distance. As previously noted, substantial upward inclination of the flow is observed for negative values of z_{te}/c.

The region of upward inclination extends substantially below the shear layer and is still prominent at $x/c = 1.2$.

Figure 28 ($M = 0.84$) shows significant differences from figure 27. The boundary layer profiles are consistent with the conclusions from the surface pressure measurements, namely that the shock wave has moved downstream to a location between $x/c = 0.70$ and 0.80, so that the boundary layer profile at the latter station is now nearly separated and that at the former station is quite full. Also, the trailing edge separation and its apparent decambering effect have become more severe.

The Nature of the Separation

It is instructive to examine the present results in the system of categorizing transonic airfoil flow fields proposed by Pearcey *et al.*, reference 19. When no trailing-edge separation occurs until the shock-induced separated region extends to the trailing edge, the situation is referred to as Type A. If trailing-edge separation is either the sole mode of separation or occurs before the reattachment point of a shock-induced separated region has reached the trailing edge, it is called Type B. The evolution of the flow field about the DSMA 523 airfoil section at supercritical Mach numbers is clearly Type B.

In the present situation, the upper-surface shock moves aft as the freestream Mach number increases, as would be expected. The local Mach number upstream of the shock remains nearly constant, at 1.2 to 1.25. Both the surface static pressure data and the limited probe data imply that little, if any, separation occurs at the foot of the shock. Both types of data also indicate that the flow is entirely subsonic downstream of the shock for $M \geqslant 0.83$. This picture is correct even after the drag coefficient has increased greatly (at Mach 0.84) relative to its subcritical value. The boundary-layer data at $M = 0.83$ show a nearly-separated profile just downstream of the shock, which recovers to a fuller profile with increased skin friction as it moves downstream in the short, constant-pressure region. Separation occurs just upstream of the trailing edge, following a region of strong adverse pressure gradient. As the Mach number is increased to 0.84 (in this case also accompanied by a small increase in lift coefficient), the shock moves aft, eliminating the region of nearly constant pressure between the shock and the trailing edge. Therefore, the boundary layer encounters adverse pressure gradients associated both with the shock wave and with the trailing edge flow in quick succession. The extent of the trailing edge separation is significantly increased by the nearness of the shock compression.

A separation criterion discussed by Alber (ref. 23) and Alber *et al.* (ref. 24) is that pressure-gradient-induced separation will occur when $-(\theta/u_e)(du_e/dx) > 0.004$. Sufficient data to allow comparisons with this criterion were obtained for two test conditions: $M = 0.83$, $c_l = 0.54$, and $M = 0.84$, $c_l = 0.58$ (see figs. 27 and 28). In the first instance, this parameter reached a maximum value of 0.0038 at $x/c = 0.95$. Since a small region of trailing-edge separation was present, fair agreement with the criterion existed in this case. In the second instance, associated with a substantially larger region of separation, the maximum value of this quantity was approximately 0.0029 at $x/c = 0.9$. This result must be regarded as rather poor agreement with the criterion. It is possible that this disagreement may be related to the proximity of the shock to the separation line.

Transonic Airfoil Calculations and Data

It was noted earlier that a number of finite difference computer programs for calculating inviscid transonic flow fields are in the repertory (e.g., refs. 9–11). Viscous effects may be approximated by the addition of some boundary layer displacement correction.

A measured pressure distribution at $M = 0.80$, $c_l = 0.54 \pm 0.01$, compared with results calculated by the Caughey program (ref. 11), is presented in figure 29. There are two computed distributions: (1) without boundary layer included, and (2) with boundary layer thickening, $\delta^*(x)/c$, included as measured during the tests on the upper surface and as estimated by the Cebeci program (ref. 22) on the lower surface.

Even when the boundary layer is included, the calculation does not compare very well with the measurements, the chief differences being that the experimental pressure distribution shows less lower surface suction (more lift) and a more forward upper surface shock wave (less lift, compensating). Some inaccuracy should be expected in the lower surface pressures, as the Cebeci program would not predict boundary layer thickening or separation in the concavity. It should also be mentioned that this case is a difficult test for any calculation scheme; the upper surface shock traverses a large portion of the chord during a few hundredths variation in Mach number.

The pressure distribution computed assuming no boundary layer is very inaccurate. The effective camber is greatly exaggerated by such an assumption, and this leads to over-estimated upper surface suction, and a stronger, more rearward shock wave.

Related drag-rise results, measured and calculated, are shown in figure 30. From the boundary layer drag curve, it is concluded that the changes (with Mach number) in viscous dissipation within the boundary layer are not sufficient to explain the transonic drag rise. Instead, the Caughey program with boundary layer correction predicts a wave drag increase on the airfoil that compares well with the experiment. The computation of drag on the airfoil without the boundary layer compares poorly with the experiment, showing a much earlier drag increase than was measured. This is consistent with the surface pressure distribution results; unless the boundary layer is included in the airfoil profile definition, the calculation predicts stronger, drag-producing shock waves.

Since the present airfoil was (in effect) designed with a boundary layer included, namely by iterative experiments in a wind tunnel, it is not surprising that this profile and its performance are de-optimized by the mathematical removal of the boundary layer. At the high Mach numbers, however, the boundary layer separates from the upper surface (fig. 13), and this separation certainly contributes to the drag increase.

Three-Dimensionality

Center-span pressure distributions together with measured spanwise variances, for several flow conditions, are given in figure 31. The deviations are worse for the essentially transonic cases ($M \geqslant 0.8$) than for the essentially subsonic case ($M = 0.6$). The magnitudes of some of the variances can be accounted for only by postulating a spanwise warpage of the shock wave. It is recalled that some of the schlieren photographs indicated rather diffuse shock fronts (fig. 8) that apparently

represent both unsteadiness and nonuniformity in the average spanwise position. Only the latter can show up in the (slow-response) surface pressure distributions.

Figure 32 shows spanwise distributions of trailing edge pressure for several flow conditions. Again, the nonuniformity is greater for the higher Mach numbers. In particular, the $M = 0.86$ data show both positive and negative C_{pte} at different spanwise locations. This case clearly exhibits trailing edge separation at the center span; apparently the phenomenon is cellular in nature, as suggested by the oil flow observations of reference 16.

Figure 33 presents spanwise-displaced trailing edge boundary layer profiles (in speed magnitude and direction) for both $M = 0.60$ and $M = 0.80$; neither case is considered separated. It is seen that the deviation is much greater at the higher Mach number, whether measured by speed or by angularity. This is so in spite of the fact that the lower Mach number case carries a higher c_l, manifest in a larger overall pressure rise and a much thicker upper surface boundary layer.

The measurements discussed above are typical of the data acquired. At the higher (supercritical) Mach numbers, for which lateral propagation of disturbances is effective, significant three-dimensional effects are consistently present in the nominally two-dimensional tests.

CONCLUDING REMARKS

As the Mach number is increased above 0.80, the DSMA 523 supercritical profile develops a variety of substantial shock wave patterns involving both the upper and lower surfaces, depending on the value of section lift coefficient. For section lift coefficients of 0.5 to 0.6, increasing upper surface separation is associated with increasing Mach number, strengthening shock wave, and increasing lift coefficient. This separation is fundamentally the trailing-edge type rather than that resulting from the growth of a shock-induced bubble. It produces an effective reduction in the camber of the profile. On the lower surface, a separation bubble may have been present in the concavity. Upon reaching the trailing edge, the lower surface streamlines curve sharply upward, to enclose a dead-water region produced by the trailing edge bluntness and by the upper surface separation.

Inviscid transonic finite difference calculations can produce results of acceptable accuracy, with regard to both lift and drag, if and only if a modeling of the viscous effects discussed above is provided.

Transonic boundary layer finite-difference calculations can be done accurately so long as rapid compressions do not occur in the upstream vicinity of the station considered. Measured profiles conform well with combined law-of-the-wall and law-of-the-wake functions.

Significant three-dimensional effects are noted in the data measured at supercritical Mach numbers. Therefore, flow field survey and surface pressure data must always be taken in the same spanwise plane, and matched at fixed section lift coefficient rather than model angle of attack.

From a contemplation of further tests, it has been determined that certain more advanced instrumentation, including surface flow visualization and minimum-interference improved-flow-field

point measurement techniques could be usefully applied to the present type studies. Such improved techniques should be applied to the measurement of the flow field characteristics of the lower surface concavity of the present profile. Data sampling at other flow conditions would enhance understanding of the results so far; specifically, (1) measurements at higher or simulated-higher Reynolds numbers to approximate flight conditions, or measurements to determine the degree to which data obtained in the Reynolds number range of the present experiments are representative of flight conditions, and (2) measurements in subcritical, non-separated cases to test computational methods. Experiments on one or more modified profiles, with trailing edge contours reworked with a view toward delaying or alleviating the rapid drag rise, would stand as an empirical approach to the design of improved transonic airfoil sections.

Ames Research Center
National Aeronautics and Space Administration
Moffett Field, Calif., 94035, April 1, 1975

REFERENCES

1. Whitcomb, Richard T.: Review of NASA Supercritical Airfoils. ICAS Paper No. 74-10, presented at the 9th Congress of the Intl. Council of Aeron. Sci., Haifa, Israel, Aug. 25-30, 1974.

2. Harris, Charles D.: Wind-Tunnel Investigation of Effects of Trailing-Edge Geometry on a NASA Supercritical Airfoil Section. NASA TM X-2336, 1971.

3. Harris, Charles D.: Aerodynamic Characteristics of Two 10-Percent-Thick NASA Supercritical Airfoils With Different Upper Surface Curvature Distributions. NASA TM X-2977, 1974.

4. Supercritical Wing Technology: A Progress Report on Flight Evaluations. NASA-SP-301, 1972.

5. Ayers, Theodore G.: Supercritical Aerodynamics Worthwhile Over a Range of Speeds. Astronaut. & Aeronaut., vol. 10, no. 8, Aug. 1972, pp. 32–36.

6. Yoshihara, Hideo; Carter, Wilbert V.; Fatta, G. Joseph; Magnus, Richard J.; and Murray, Robert T.: Aeronautical Exploratory Research on Advanced Jet Flap Supercritical Airfoils. General Dynamics/Convair Interim Technical Report 3/71–2/72, AD744036, Feb. 1972.

7. Tranen, T. L.: A Rapid Computer Aided Transonic Airfoil Design Method. AIAA (Preprint) 74-501, June 1974.

8. Sewell, A. E.: The Results of Two-Dimensional Airfoil Tests Conducted in the Ames Six-Foot Wind Tunnel During 1969 and 1970. McDonnell Douglas Report MDCJ5056, May 1973.

9. Krupp, J. A.; and Murman, E. M.: Computation of Transonic Flows Past Lifting Airfoils and Slender Bodies. AIAA J., vol. 10, no. 7, July 1972, pp. 880–886.

10. Garabedian, P. R.; and Korn, D. G.: Analysis of Transonic Airfoils. Commun. Pure & Appl. Math., vol. 24, no. 11, Nov. 1971, pp. 841–851.

11. Caughey, D. A.: Users' Guide for CPROX: A Transonic Airfoil Analysis Program. McDonnell Douglas Report MDCQ0506, Dec. 1973.

12. Evans, W.; MacKenzie, D.; and Romanowski, R.: The Design, Test and Evaluation of Shockless Transonic Airfoils. U.S. Navy Final Report, Contract No. N00019-72-C-03580, Grumman Aerospace Corp., Sept. 1973.

13. Hurley, F. X.; and Roos, F. W.: Experimental Study of the Flow Field About an Advanced Transonic Airfoil. McDonnell Douglas Report MDC Q0479, Dec. 1973.

14. Cook, T. A.: Measurements of the Boundary Layer and Wake of Two Aerofoil Sections at High Reynolds Numbers and High-Subsonic Mach Numbers. Technical Report 71127, British R.A.E., 1971.

15. Vidal, R. J.; Wittliff, C. E.; Catlin, P. A.; and Sheen, B. H.: Reynolds Number Effects on the Shock Wave-Turbulent Boundary Layer Interaction at Transonic Speeds. AIAA (Preprint) 73-661, July 1973.

16. Gregory, N.; Quincy, V. G.; O'Reilly, C. L.; and Hall, D. J.: Progress Report on Observations of Three-Dimensional Flow Patterns Obtained During Stall Development on Aerofoils, and on the Problem of Measuring Two-Dimensional Characteristics. Progress Report NPL-AERO-1309, 1970.

17. Bryer, D. W.; and Pankhurst, R. C.: Pressure-Probe Methods for Determining Wind Speed and Flow Direction. Her Majesty's Stationery Office (London), 1971.

18. Braslow, Albert L.; Hicks, Raymond M.; and Harris, Roy V., Jr.: Use of Grit-Type Boundary-Layer-Transition Trips on Wind-Tunnel Models. NASA TN D-3579, 1966.

19. Pearcey, H. H.; Osborne, J.; and Haines, A. B.: The Interaction Between Local Effects at the Shock and Rear Separation – A Source of Significant Scale Effects in Wind-Tunnel Tests on Aerofoils and Wings. Proceedings of the AGARD Conference on Transonic Aerodynamics. AGARD-CP-35, Sept. 1968.

20. Coles, D. E.: The Young Person's Guide to the Data. Proceedings: Computation of Turbulent Boundary Layers. 1968 AFOSR-IFP-Stanford Conference, Vol. II, Compiled Data, D. E. Coles and E. A. Hirst, eds., Stanford University, 1969.

21. van Driest, E. R.: Turbulent Boundary Layer in Compressible Fluids. J. Aeronaut. Sci., vol. 18, no. 3, Mar. 1951, pp. 145–160.

22. Cebeci, T.; Smith, A. M. O.; and Wang, L. C.: A Finite Difference Method for Calculating Compressible Laminar and Turbulent Boundary Layers, Part I. McDonnell Douglas Report DAC-67131, Mar. 1969.

23. Alber, I. E.: Similar Solutions for a Family of Separated Turbulent Boundary Layers. AIAA (Preprint) 71-203, Jan. 1971.

24. Alber, I. E.; Bacon, J. W.; Masson, B. S.; and Collins, D. J.: An Experimental Investigation of Turbulent Transonic Viscous-Inviscid Interactions. AIAA J., vol. 11, no. 5, May 1973, pp. 620–627.

TABLE 1.– DSMA 523 PROFILE COORDINATES

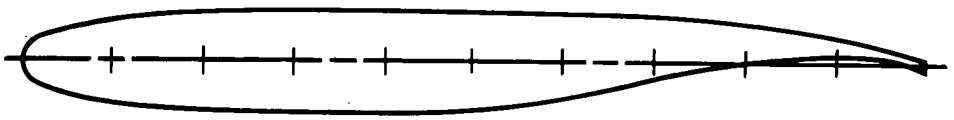

$\frac{x}{c}$	$\frac{z_{upper}}{c}$	$\frac{z_{lower}}{c}$	$\frac{x}{c}$	$\frac{z_{upper}}{c}$	$\frac{z_{lower}}{c}$
0.000500	0.005069	–0.005096	0.440000	0.055247	–0.053009
0.001000	0.007096	–0.007128	0.460000	0.055146	–0.052143
0.002500	0.011063	–0.011078	0.480000	0.054973	–0.051136
0.005000	0.015320	–0.015320	0.500000	0.054723	–0.049915
0.007500	0.018417	–0.018417	0.520000	0.054390	–0.048483
0.010000	0.020716	–0.020671	0.540000	0.053976	–0.046780
0.012500	0.022651	–0.022548	0.560000	0.053486	–0.044613
0.015000	0.024267	–0.024135	0.580000	0.052917	–0.042006
0.020000	0.026918	–0.026744	0.600000	0.052269	–0.038885
0.030000	0.030729	–0.030667	0.620000	0.051540	–0.035181
0.040000	0.033459	–0.033607	0.640000	0.050726	–0.030940
0.060000	0.037407	–0.038087	0.660000	0.049826	–0.026390
0.080000	0.040367	–0.041739	0.680000	0.048832	–0.021541
0.100000	0.042987	–0.044548	0.700000	0.047725	–0.016958
0.120000	0.045198	–0.046796	0.720000	0.046494	–0.012692
0.140000	0.047017	–0.048616	0.740000	0.045130	–0.008750
0.160000	0.048543	–0.050114	0.760000	0.043625	–0.005200
0.180000	0.049828	–0.051348	0.780000	0.041942	–0.002041
0.200000	0.050902	–0.052370	0.800000	0.040043	(+)0.000686
0.220000	0.051802	–0.053207	0.820000	0.037907	0.002965
0.240000	0.052563	–0.053890	0.840000	0.035502	0.004757
0.260000	0.053199	–0.054423	0.860000	0.032780	0.006021
0.280000	0.053729	–0.054808	0.880000	0.029666	0.006687
0.300000	0.054161	–0.055056	0.900000	0.026155	0.006606
0.320000	0.054513	–0.055163	0.920000	0.022185	0.005630
0.340000	0.054788	–0.055137	0.940000	0.017708	0.003565
0.360000	0.054998	–0.054978	0.960000	0.012642	(+)0.000348
0.380000	0.055149	–0.054701	0.980000	0.006842	–0.004210
0.400000	0.055240	–0.054283	1.000000	(+)0.000308	–0.010109
0.420000	0.055272	–0.053719	R_{le}/c = 0.023		

TABLE 2.– LIFT DATA TABULATION

(a) Test 22-744-1, transition strip at 12 percent chord

Run no.	M	$Re_c \times 10^{-6}$	α rad (deg)		c_l	α_{geom} rad (deg)	
71-895	0.882	3.9	−0.023	(−1.32)	−0.033	−0.025	(−1.43)
71-896	0.882	4.0	−0.001	(−0.06)	0.074	0.003	(0.18)
71-897	0.876	4.0	0	(−0.02)	0.122	0.007	(0.38)
72-903	0.860	3.0	−0.022	(−1.27)	−0.037	−0.024	(−1.39)
72-904	0.860	3.0	−0.009	(−0.50)	0.105	−0.003	(−0.16)
72-906	0.843	3.0	−0.010	(−0.57)	0.322	0.008	(0.48)
73-908	0.839	3.0	−0.024	(−1.37)	−0.013	−0.025	(−1.41)
73-909	0.838	3.0	−0.014	(−0.81)	0.307	0.004	(0.20)
74-910	0.773	1.0	−0.034	(−1.97)	0.170	−0.025	(−1.41)
75-911	0.888	1.0	−0.002	(−0.10)	0.179	0.008	(0.48)
76-912	0.825	3.0	−0.026	(−1.47)	0.018	−0.025	(−1.42)
76-913	0.819	3.0	−0.014	(−0.80)	0.393	0.008	(0.48)
77-914	0.799	3.0	−0.016	(−0.92)	0.344	0.004	(0.20)
77-915	0.803	3.0	−0.014	(−0.81)	0.400	0.009	(0.49)
78-924	0.820	3.0	−0.013	(−0.73)	0.468	0.014	(0.80)
78-925	0.818	3.0	−0.012	(−0.71)	0.467	0.014	(0.81)
78-926	0.820	3.0	−0.011	(−0.61)	0.551	0.021	(1.19)
78-927	0.819	3.0	−0.008	(−0.46)	0.599	0.026	(1.49)
79-928	0.799	3.0	−0.013	(−0.72)	0.464	0.014	(0.79)
79-929	0.801	3.0	−0.010	(−0.58)	0.544	0.021	(1.19)
79-930	0.800	3.0	−0.008	(−0.48)	0.606	0.026	(1.49)
80-936	0.844	3.0	−0.007	(−0.37)	0.466	0.020	(1.15)
80-938	0.840	3.0	−0.003	(−0.19)	0.519	0.026	(1.51)
81-940	0.774	3.0	−0.012	(−0.70)	0.460	0.014	(0.80)
81-941	0.774	3.0	−0.010	(−0.56)	0.539	0.021	(1.19)
81-942	0.774	3.0	−0.008	(−0.46)	0.571	0.024	(1.39)
82-943	0.821	3.0	−0.014	(−0.78)	0.429	0.011	(0.62)
82-944	0.820	3.0	−0.011	(−0.65)	0.503	0.017	(1.00)
83-946	0.839	3.0	−0.012	(−0.70)	0.404	0.011	(0.62)
83-948	0.838	3.0	−0.009	(−0.52)	0.460	0.017	(0.98)

TABLE 2.– Continued.

(b) Test 22-700-2, leading edge transition band

Run no.	M	$Re_c \times 10^{-6}$	α rad (deg)	c_l	α_{geom} rad (deg)
3-27	0.826	3.0	−0.014 (−0.80)	0.556	0.018 (1.02)
5-45	0.598	2.0	0.042 (2.40)	0.829	0.087 (5.00)
6-52	0.871	2.0	−0.003 (−0.19)	0.458	0.023 (1.30)
8-72	0.868	2.0	−0.003 (−0.18)	0.451	0.023 (1.30)
9-73	0.819	2.0	−0.014 (−0.82)	0.540	0.016 (0.94)
11-88	0.819	2.0	−0.014 (−0.79)	0.531	0.017 (0.95)
12-89	0.819	2.0	−0.011 (−0.60)	0.634	0.026 (1.47)
14-104	0.818	2.0	−0.011 (−0.60)	0.639	0.026 (1.49)
15-105	0.820	2.0	−0.008 (−0.45)	0.717	0.033 (1.90)
17-121	0.820	2.0	−0.008 (−0.43)	0.713	0.033 (1.90)
18-122	0.819	2.0	−0.016 (−0.89)	0.486	0.012 (0.70)
20-139	0.817	2.0	−0.014 (−0.82)	0.466	0.012 (0.70)
21-141	0.822	2.0	−0.012 (−0.71)	0.570	0.020 (1.15)
25-177	0.798	2.0	−0.013 (−0.75)	0.525	0.017 (0.96)
26-178	0.749	2.0	−0.012 (−0.67)	0.497	0.017 (0.95)
29-204	0.839	2.0	−0.010 (−0.59)	0.577	0.023 (1.30)
30-207	0.820	2.0	−0.015 (−0.86)	0.476	0.012 (0.70)
30-208	0.821	2.0	−0.016 (−0.89)	0.488	0.012 (0.70)
31-210	0.821	2.0	−0.015 (−0.84)	0.545	0.016 (0.94)
32-211	0.817	2.0	−0.013 (−0.76)	0.586	0.020 (1.16)
33-212	0.820	2.0	−0.011 (−0.63)	0.641	0.026 (1.47)
34-213	0.820	2.0	−0.007 (−0.41)	0.708	0.033 (1.91)
35-215	0.802	2.0	−0.014 (−0.79)	0.528	0.016 (0.93)
36-216	0.821	2.0	−0.014 (−0.79)	0.555	0.018 (1.02)
37-218	0.811	2.0	−0.014 (−0.79)	0.530	0.016 (0.94)
38-219	0.833	2.0	−0.013 (−0.76)	0.547	0.018 (1.03)
39-220	0.749	2.0	−0.012 (−0.69)	0.508	0.017 (0.96)
40-243	0.799	2.0	−0.014 (−0.79)	0.533	0.017 (0.95)
40-245	0.797	2.0	−0.014 (−0.81)	0.540	0.016 (0.94)
41-247	0.820	2.0	−0.015 (−0.85)	0.550	0.016 (0.94)
42-249	0.839	2.0	−0.011 (−0.63)	0.592	0.023 (1.30)
43-250	0.599	2.0	0.037 (2.13)	0.918	0.088 (5.02)
44-251	0.838	2.0	0.008 (0.48)	0.774	0.053 (3.01)
45-252	0.819	3.0	−0.007 (−0.39)	0.641	0.030 (1.70)

TABLE 2.– Continued.

(b) Test 22-700-2, leading edge transition band – Continued.

Run no.	M	$Re_c \times 10^{-6}$	α rad (deg)		c_l	α_{geom} rad (deg)	
46-254	0.818	3.0	−0.012	(−0.71)	0.514	0.017	(0.97)
47-255	0.821	3.0	−0.014	(−0.78)	0.423	0.011	(0.60)
48-256	0.839	3.5	−0.009	(−0.54)	0.472	0.017	(1.00)
49-258	0.819	3.5	−0.012	(−0.70)	0.518	0.017	(1.00)
50-259	0.821	3.5	−0.013	(−0.77)	0.421	0.011	(0.60)
51-260	0.819	3.5	−0.017	(−0.98)	0.296	0	(−0.01)
52-265	0.841	2.0	−0.011	(−0.60)	0.582	0.023	(1.30)
53-266	0.833	2.0	−0.012	(−0.71)	0.586	0.021	(1.21)
54-268	0.832	2.0	−0.007	(−0.40)	0.656	0.031	(1.75)
55-269	0.821	2.0	−0.003	(−0.18)	0.760	0.040	(2.30)
56-270	0.866	2.0	−0.003	(−0.19)	0.458	0.023	(1.31)
57-271	0.874	2.0	−0.002	(−0.11)	0.431	0.023	(1.30)
58-273	0.819	2.0	−0.015	(−0.83)	0.542	0.017	(0.95)
59-275	0.870	2.0	−0.002	(−0.09)	0.424	0.023	(1.30)
60-277	0.821	2.0	−0.015	(−0.84)	0.538	0.016	(0.92)
61-278	0.868	2.0	−0.003	(−0.15)	0.444	0.023	(1.30)
62-279	0.819	2.0	−0.015	(−0.83)	0.542	0.017	(0.95)
63-280	0.867	2.0	−0.002	(−0.14)	0.442	0.023	(1.30)
64-281	0.846	4.0	−0.001	(−0.07)	0.424	0.023	(1.32)
65-282	0.820	4.0	−0.014	(−0.78)	0.527	0.016	(0.94)
66-283	0.870	4.0	−0.014	(−0.78)	0.086	−0.009	(−0.50)
67-284	0.823	3.0	−0.025	(−1.43)	0.130	−0.017	(−1.00)
68-285	0.821	3.0	−0.029	(−1.64)	0.040	−0.026	(−1.51)
69-286	0.778	3.0	−0.033	(−1.91)	0.121	−0.026	(−1.51)
70-287	0.775	3.0	−0.028	(−1.62)	0.189	−0.017	(−1.00)
72-322	0.599	2.0	0.037	(2.12)	0.922	0.088	(5.02)
74-356	0.749	3.0	−0.012	(−0.68)	0.506	0.017	(0.97)
77-401	0.800	3.0	−0.013	(−0.76)	0.518	0.016	(0.92)
80-460	0.818	3.0	−0.013	(−0.77)	0.518	0.016	(0.92)
82-489	0.600	2.0	0.037	(2.14)	0.904	0.087	(4.98)
86-579	0.858	3.0	−0.005	(−0.27)	0.479	0.023	(1.30)
89-641	0.838	3.0	−0.012	(−0.68)	0.518	0.018	(1.01)
90-642	0.840	3.0	−0.009	(−0.54)	0.561	0.023	(1.30)
92-684	0.858	3.0	−0.005	(−0.29)	0.488	0.018	(1.30)

TABLE 2.– Concluded.

(b) Test 22-700-2, leading edge transition band – Concluded.

Run no.	M	$Re_c \times 10^{-6}$	α rad (deg)		c_l	α_{geom} rad (deg)	
95-763	0.836	3.0	−0.0010	(−0.59)	0.577	0.023	(1.30)
97-811	0.599	2.0	0.038	(2.15)	0.908	0.087	(5.00)
99-853	0.829	3.0	−0.013	(−0.74)	0.545	0.018	(1.04)
101-886	0.750	3.0	−0.012	(−0.70)	0.513	0.017	(0.96)
104-952	0.818	3.0	−0.014	(−0.78)	0.527	0.016	(0.94)
106-975	0.801	3.0	−0.013	(−0.77)	0.527	0.017	(0.95)
109-1036	0.830	3.0	−0.013	(−0.72)	0.537	0.018	(1.03)
117-1188	0.801	3.0	−0.013	(−0.73)	0.510	0.016	(0.93)
118-1189	0.751	3.0	−0.012	(−0.68)	0.506	0.017	(0.96)
119-1190	0.599	2.0	0.037	(2.13)	0.911	0.087	(4.99)
120-1191	0.860	3.0	−0.005	(−0.27)	0.487	0.023	(1.32)
123-1267	0.831	3.0	−0.011	(−0.61)	0.584	0.023	(1.30)
125-1308	0.827	3.0	−0.014	(−0.78)	0.544	0.017	(1.00)

TABLE 3.– DRAG DATA TABULATION

(a) Test 22-744-1, transition strip at 12 percent chord; drag rake

Run no.	$Re_c \times 10^{-6}$	c_l	M	c_d	$(x - x_{te})/c^a$	Notes
71	3.9	–0.033	0.882	0.0500	1.75	
71	4.0	0.074	0.882	0.0485	1.75	
71	4.0	0.122	0.876	0.0479	1.75	
72	3.0	–0.037	0.860	0.0424	1.75	
72	3.0	0.105	0.860	0.0393	1.75	
72	3.0	0.322	0.843	0.0226	1.75	
73	3.0	–0.013	0.839	0.0323	1.75	
73	3.0	0.307	0.838	0.0173	1.75	
74	1.0	0.170	0.773	0.0169	1.75	
75	1.0	0.179	0.888	0.0560	1.75	
76	3.0	0.018	0.825	0.0246	1.75	
76	3.0	0.393	0.819	0.0154	1.75	
77	3.0	0.344	0.799	0.0149	1.75	
77	3.0	0.400	0.803	0.0147	1.75	
78	3.0	0.467	0.818	0.0156	1.75	
78	3.0	0.551	0.820	0.0172	1.75	
78	3.0	0.599	0.819	0.0192	1.75	
79	3.0	0.464	0.799	0.0153	1.75	
79	3.0	0.544	0.801	0.0156	1.75	
79	3.0	0.606	0.800	0.0161	1.75	
80	3.0	0.4 approx	0.840	0.0223	1.75	Lost c_l data.
80	3.0	0.466	0.844	0.0255	1.75	
80	3.0	0.519	0.840	0.0268	1.75	
81	3.0	0.460	0.774	0.0142	1.75	
81	3.0	0.539	0.774	0.0153	1.75	
81	3.0	0.571	0.774	0.0156	1.75	
82	3.0	0.429	0.821	0.0156	1.75	
82	3.0	0.503	0.820	0.0161	1.75	
83	3.0	0.404	0.839	0.0200	1.75	
83	3.0	0.460	0.838	0.0211	1.75	

[a]Location of drag rake downstream of airfoil trailing edge.

TABLE 3.– Concluded.

(b) Test 22-700-1/2, leading edge transition band; triple probe

Run no.	$Rc_c \times 10^{-6}$	c_l	M	c_d	$(x - x_{te})/c^a$	Notes
2	3.0	0.823	0.830	0.0170	0.30	Coarse traverse
7	2.0	0.455	0.869	0.0314	0.30	
10	2.0	0.535	0.819	0.0155	0.30	
13	2.0	0.636	0.822	0.0174	0.30	
16	2.0	0.715	0.819	0.0173	0.30	
19	2.0	0.476	0.819	0.0150	0.30	
24	2.0	0.525	0.799	0.0148	0.30	
27	2.0	0.497	0.748	0.0149	0.30	
28	2.0	0.577	0.839	0.0216	0.30	
129	3.0	0.537	0.830	0.0154	0.20	No transition band, rough surface finish, series 1.
130	3.0	0.527	0.800	0.0140	0.20	
131	3.0	0.537	0.830	0.0172	0.50	
138	2.0	0.473	0.837	0.0175	0.85	
142	2.0	0.249	0.799	0.0173	0.85	
143	2.0	0.508	0.750	0.0142	0.85	
147	2.0	0.522	0.797	0.0169	0.85	

[a]Location of triple probe downstream of airfoil trailing edge.

TABLE 4.– SUMMARY OF BOUNDARY LAYER PROPERTIES

				Physical coordinates					Transformed coordinates				
M	$Re_c \times 10^{-6}$	c_l	x/c[a]	δ/c	δ^*/c	θ/c	H	C_f	δ^*/c	θ/c	H	C_f^*	Π
0.86	3.0	0.48	0.70	0.0105	0.00323	0.00131	2.46	0.00224	0.00261	0.00154	1.70	0.00216	0.94
0.86	3.0	0.49	1.00	0.0710	0.04170[c]	0.00530[c]	7.88	–	0.04060[c]	0.00541[c]	6.99	–	–
0.84	3.0	0.58	0.70	0.0113	0.00251	0.00110	2.27	0.00266	0.00204	0.00127	1.61	0.00258	0.66
0.84	3.0	0.58	0.80	0.0209	0.00765	0.00283	2.70	0.00070	0.00697	0.00318	2.19	0.00067	6.07
0.84	3.0	0.58	0.90	0.0233	0.00806	0.00337	2.39	0.00086	0.00737	0.00371	1.99	0.00083	4.92
0.84	3.0	0.58	1.00	0.0416	0.02440[c]	0.00313[c]	7.79	–	0.02380[c]	0.00454[c]	7.01	–	–
0.83	3.0	0.54	0.30	0.0052	0.00095	0.00042	2.24	0.00347	0.00075	0.00049	1.55	0.00330	0.41
0.83	2.9	0.54	0.70	0.0150	0.00510	0.00200	2.55	0.00099	0.00459	0.00226	2.04	0.00096	4.50
0.83	3.0	0.54	0.80	0.0181	0.00487	0.00220	2.21	0.00169	0.00427	0.00246	1.74	0.00163	2.11
0.83	3.0	0.54	0.90	0.0228	0.00548	0.00280	1.96	0.00166	0.00484	0.00307	1.58	0.00161	2.32
0.83	3.0	0.54	0.90	0.0204	0.00563	0.00273	2.06	0.00156	0.00501	0.00300	1.67	0.00152	2.30
0.83	3.0	0.54	0.95	0.0234	0.00952	0.00378	2.59	0.00054	0.00887	0.00401	2.21	0.00053	7.19
0.83	2.9	0.54	1.00	0.0322	0.01640	0.00380	4.31	–	0.01580	0.00412	3.83	–	–
0.82	3.0	0.53	0.70	0.0160	0.00330	0.00168	1.97	0.00209	0.00282	0.00187	1.51	0.00203	1.67
0.82	3.0	0.53	1.00	0.0296	0.01470	0.00405	3.63	–	0.01410	0.00440	3.21	–	–
0.80	3.0	0.52	0.70[d]	0.0152	0.00294	0.00153	1.91	0.00253	0.00247	0.00170	1.45	0.00247	0.78
0.80	3.0	0.53	1.00	0.0254	0.01260	0.00383	3.30	–	0.01210	0.00414	2.92	–	–
0.80	3.0	0.53	0.70	0.0105	0.00272	0.00126	2.16	0.00256	0.00234	0.00139	1.68	0.00249	0.69
0.80	3.0	0.53	1.00[d]	0.0249	0.00981	0.00359	2.74	0.00048	0.00926	0.00388	2.39	0.00047	8.28
0.75	3.0	0.51	0.70	0.0120[b]	0.00208	0.00116	1.78	0.00309	0.00176	0.00127	1.39	0.00302	–
0.75	3.0	0.51	0.70[d]	0.0148	0.00275	0.00135	2.04	0.00264	0.00239	0.00148	1.62	0.00258	0.66
0.75	3.0	0.51	1.00	0.0245	0.00965	0.00410	2.36	–	0.00909	0.00439	2.07	–	–
0.60	2.0	0.90	0.70[d]	0.0580[b]	0.00763	0.00508	1.50	0.00252	0.00680	0.00536	1.27	0.00248	–
0.60	2.0	0.90	0.70[e]	0.0630[b]	0.00881	0.00568	1.55	0.00254	0.00788	0.00597	1.32	0.00250	0.34
0.60	2.0	0.92	0.70	0.0450[b]	0.01040	0.00648	1.60	0.00211	0.00934	0.00683	1.37	0.00207	–
0.60	2.0	0.90	0.70	0.0563	0.00908	0.00576	1.58	0.00244	0.00814	0.00607	1.34	0.00240	0.44

[a]Location of boundary layer probe (triple probe).

[b]Wake fit did not converge; δ determined from plot of velocity profile.

[c]Integral properties obtained from wake fit.

[d]y/c = 1.0

[e]y/c = 0.5

TABLE 5.– SUMMARY OF NEAR WAKE PROPERTIES

M	$Re_c \times 10^{-6}$	c_l	x/c [a]	δ^*/c	θ/c	H
0.837	3.0	0.584	1.050	0.0249	0.01100	2.27
0.828	3.0	0.537	1.050	0.0186	0.00921	2.02
0.830	3.0	0.537	1.100	0.0154	0.00872	1.77
0.829	3.0	0.537	1.200	0.0118	0.00770	1.54
0.830	3.0	0.537	1.500	0.0118	0.00852	1.38
0.820	3.0	0.527	1.050	0.0175	0.00887	1.98
0.800	3.0	0.527	1.050	0.0171	0.00865	1.97
0.799	3.0	0.527	1.200	0.0105	0.00695	1.50
0.600	2.0	0.908	1.000	0.0379	0.01520	2.49
0.602	2.0	0.908	1.000 [b]	0.0376	0.01460	2.58

[a] Location of triple probe.
[b] $y/c = 1.0$.

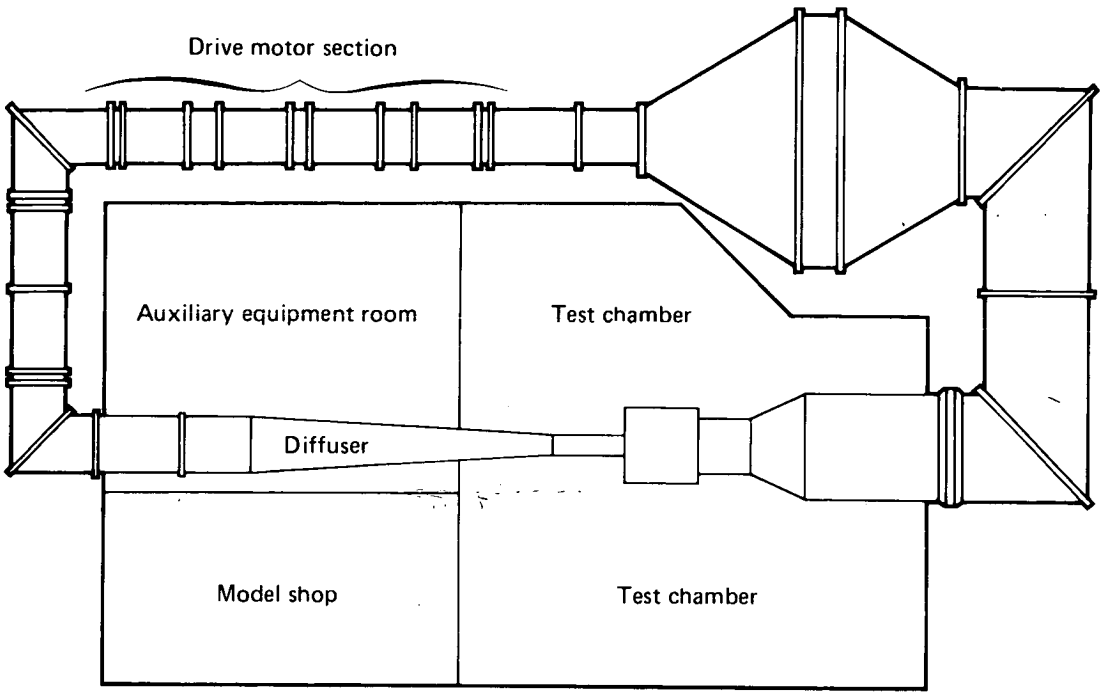

Test section configuration: 0.61m x 0.61m (2 ft x 2 ft)
Adjustable baffled slots, floor and ceiling.
Motorized, rotating thick glass discs for full span model mounting. Schlieren.
Downstream sting mount supports probe instrumentation and provides spanwise movement.

Mach number range: 0.6 to 0.95 in two-dimensional configuration (continuously variable).

Reynolds number range: Approximately 0.5×10^6 to 4×10^6 based on 15.2 cm (6 in.) chord (pressure variable).

Figure 1.– NASA Ames Two- by Two-Foot Transonic Wind Tunnel circuit and specifications.

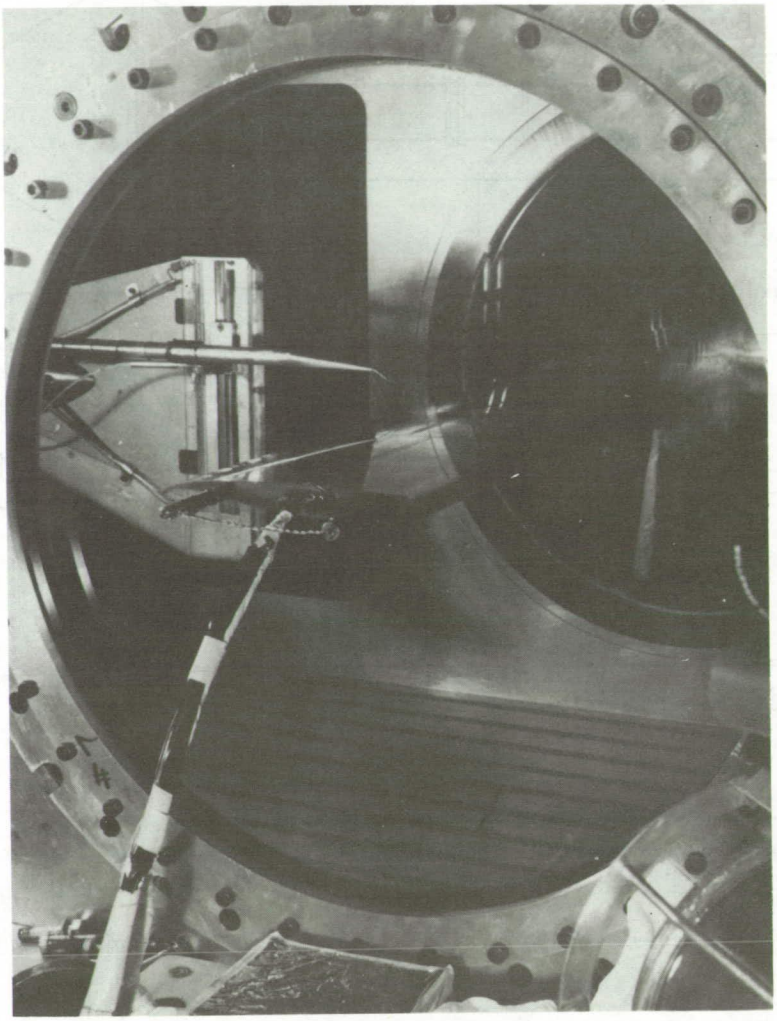

Figure 2.– NASA-Ames Two- by Two-Foot Transonic Wind Tunnel test section with MDRL probe rig and DSMA 523 airfoil model mounted for tests.

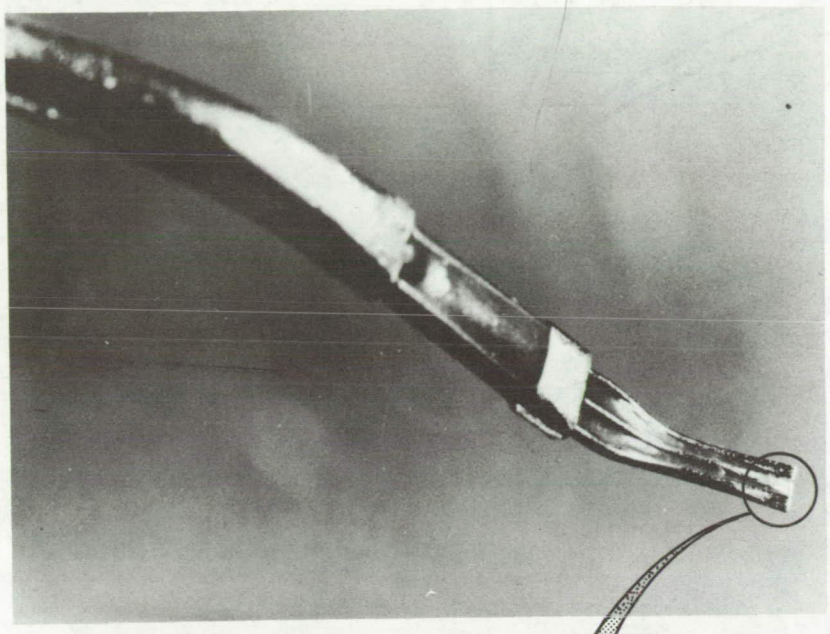

Photograph of probe

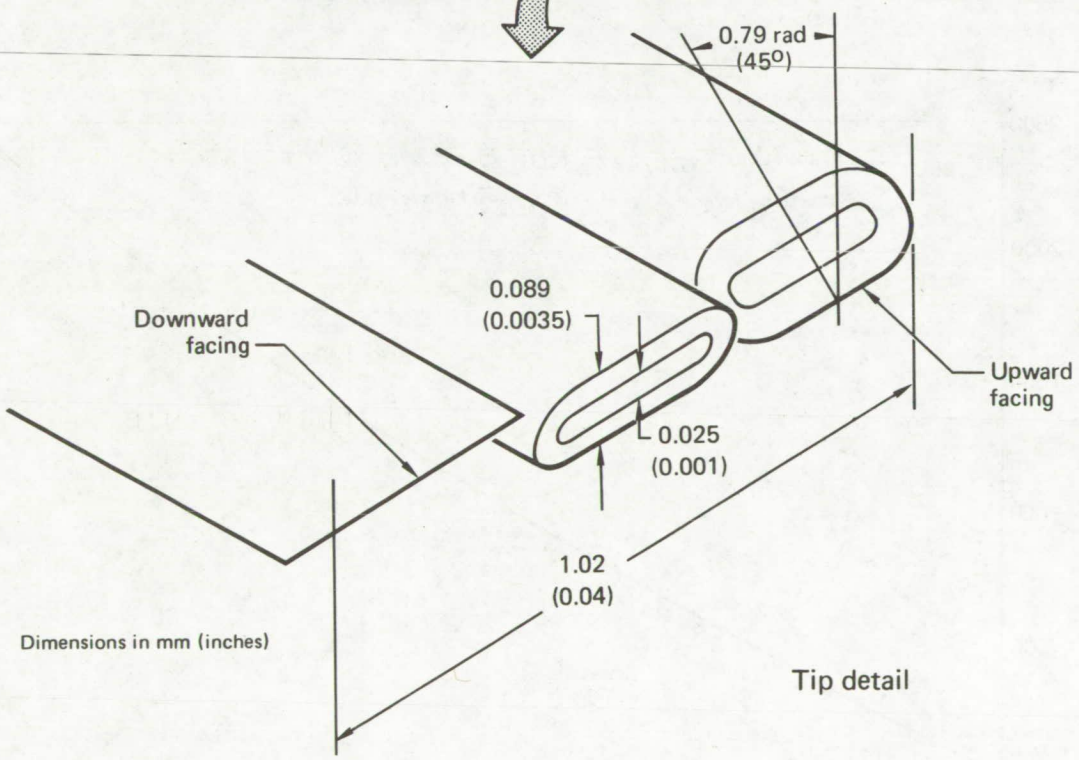

Figure 3.– Triple probe tip geometry.

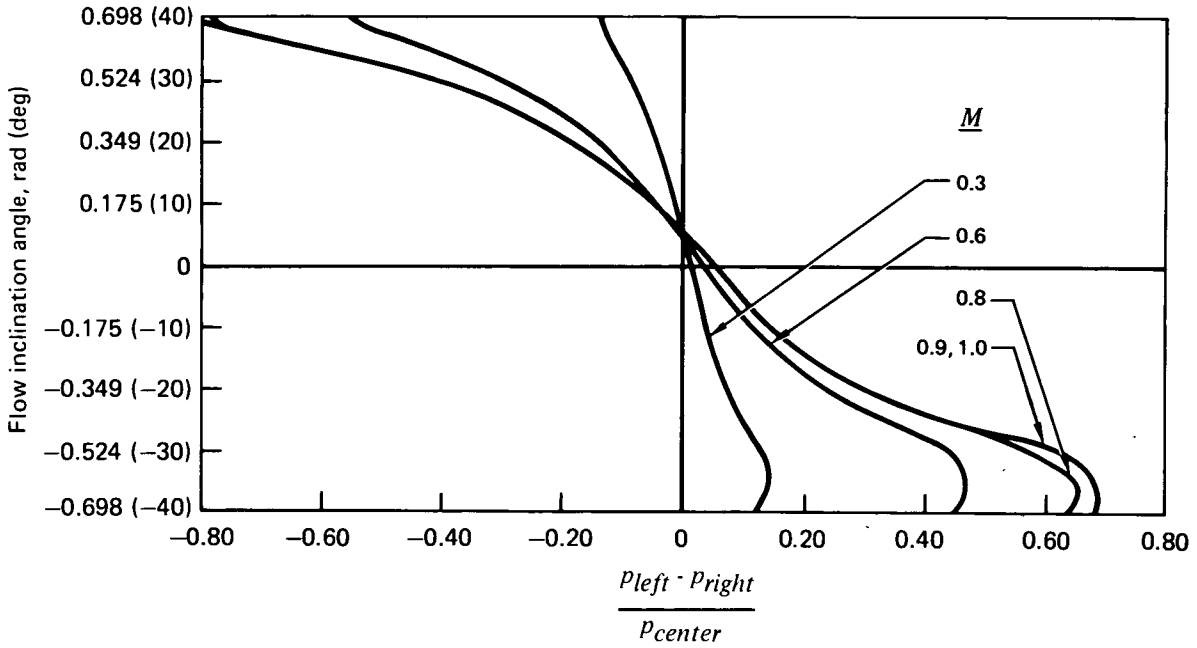

Figure 4.– Triple probe calibration curves.

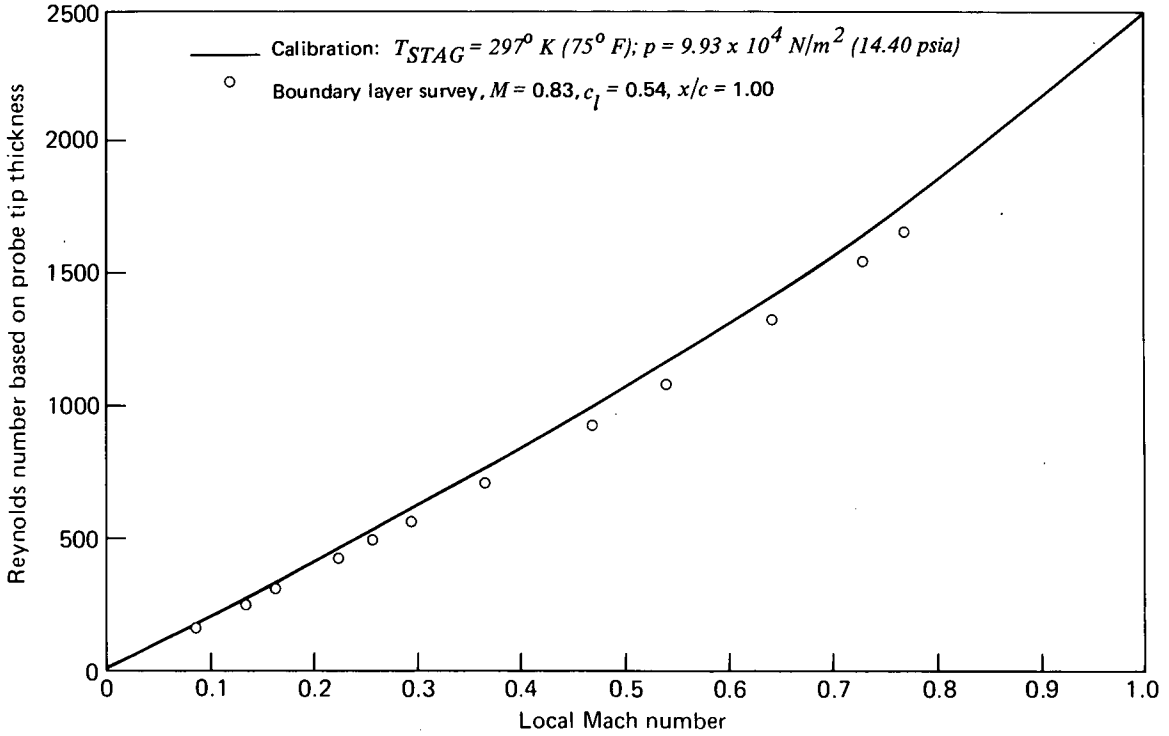

Figure 5. – Mach number-Reynolds number equivalence for probe calibration and for a typical boundary layer survey in the Ames Two- by Two-Foot Transonic Wind Tunnel.

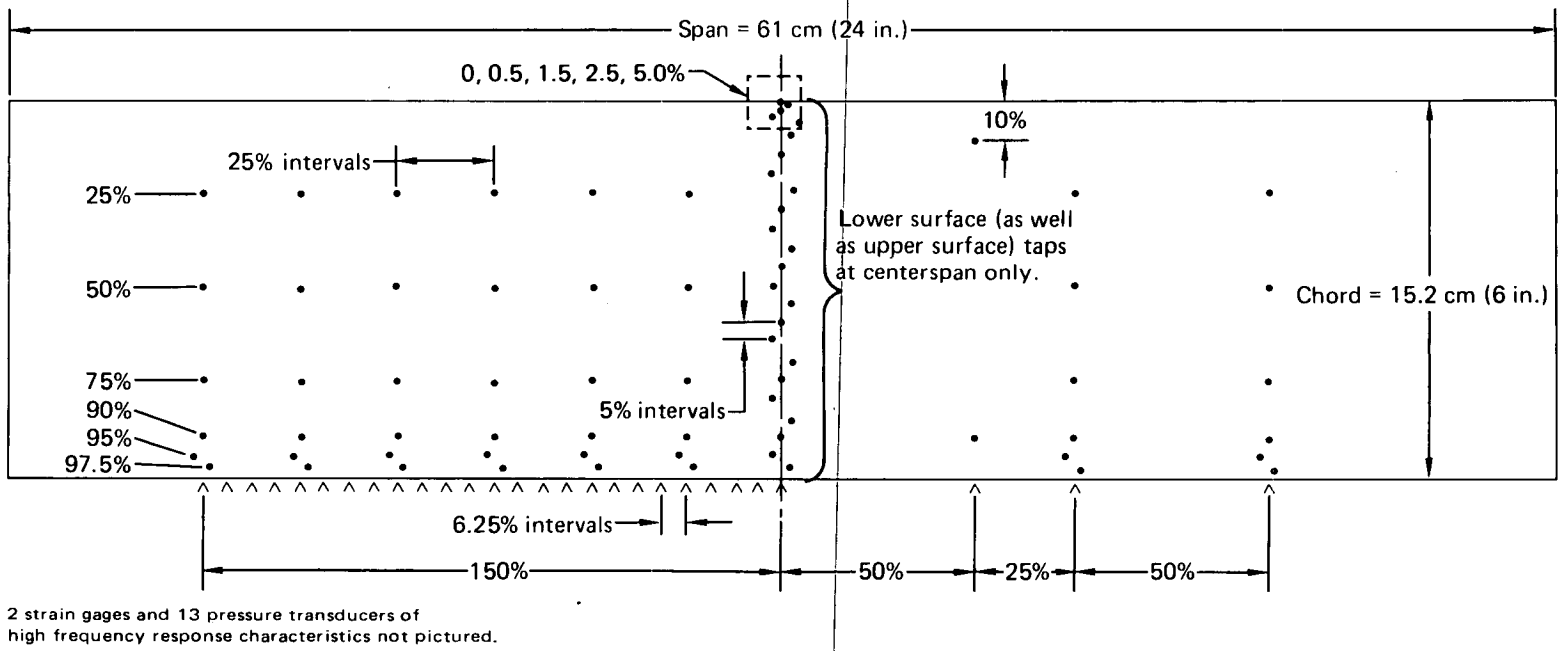

Figure 6.– Static pressure orifice array on the DSMA 523 model upper surface; dimensions in percent chord unless otherwise specified.

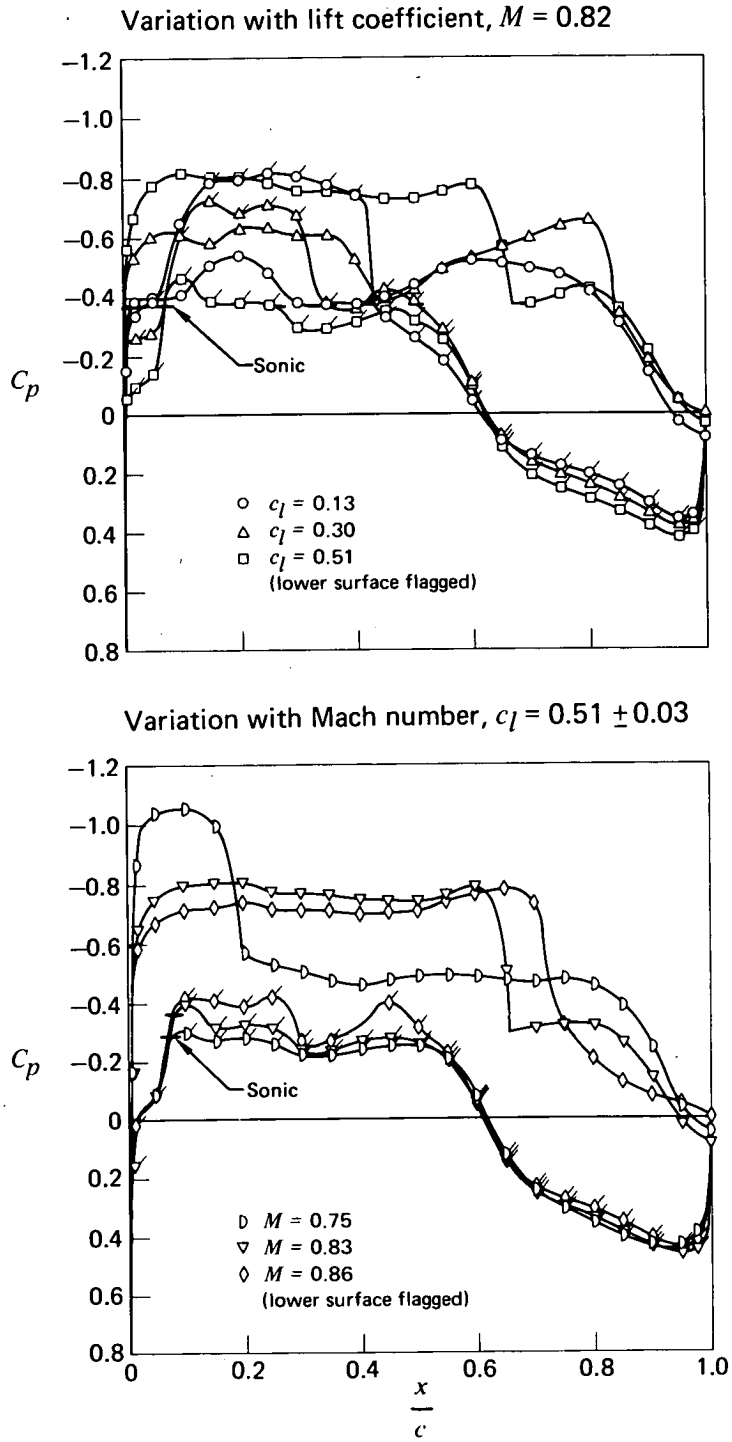

Figure 7.– Typical pressure distributions, $Re_c = 3.0 \times 10^6 - 3.5 \times 10^6$.

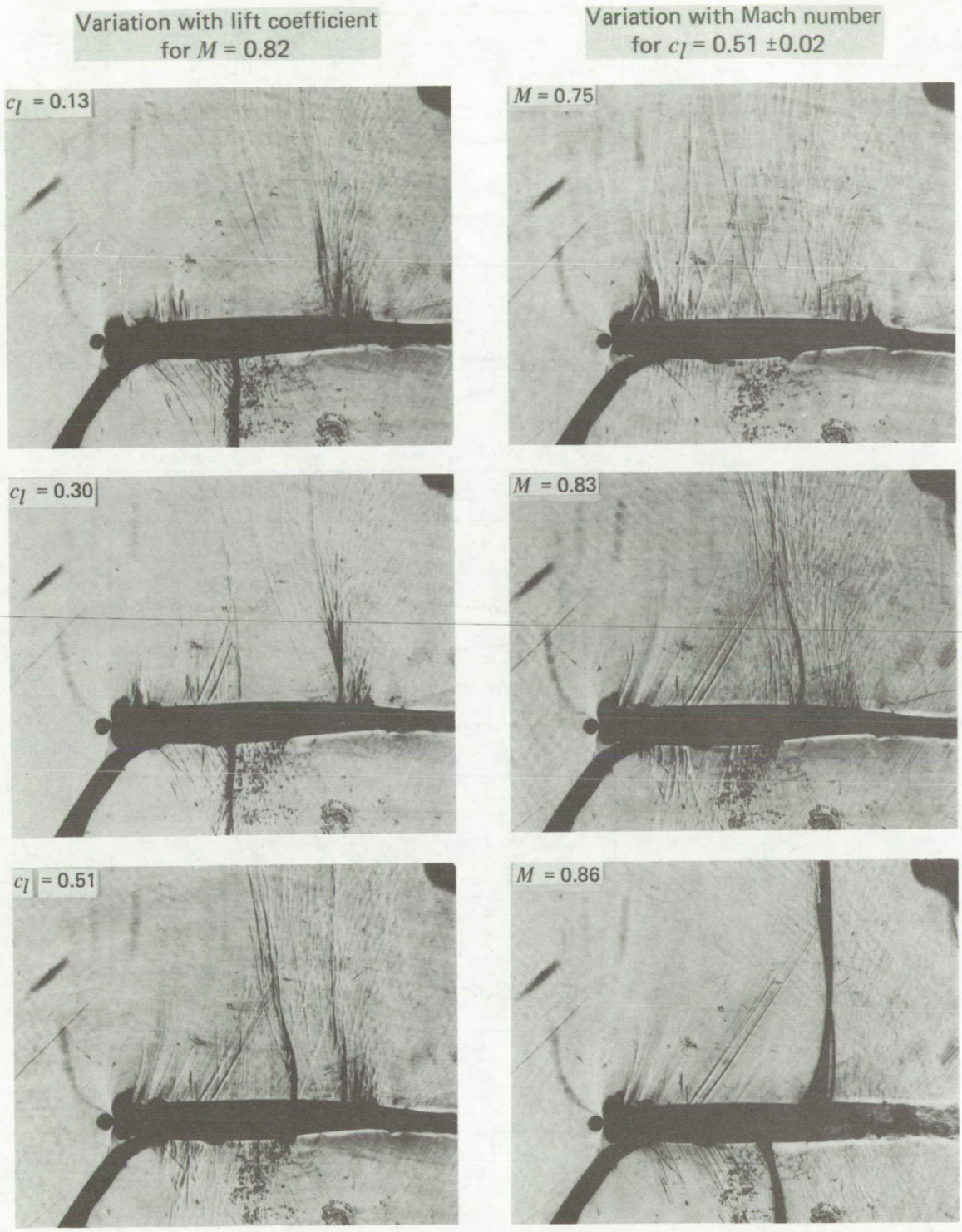

Figure 8.– Typical flow field schlieren photographs, $Re_c = 3.0 \times 10^6 - 3.5 \times 10^6$.

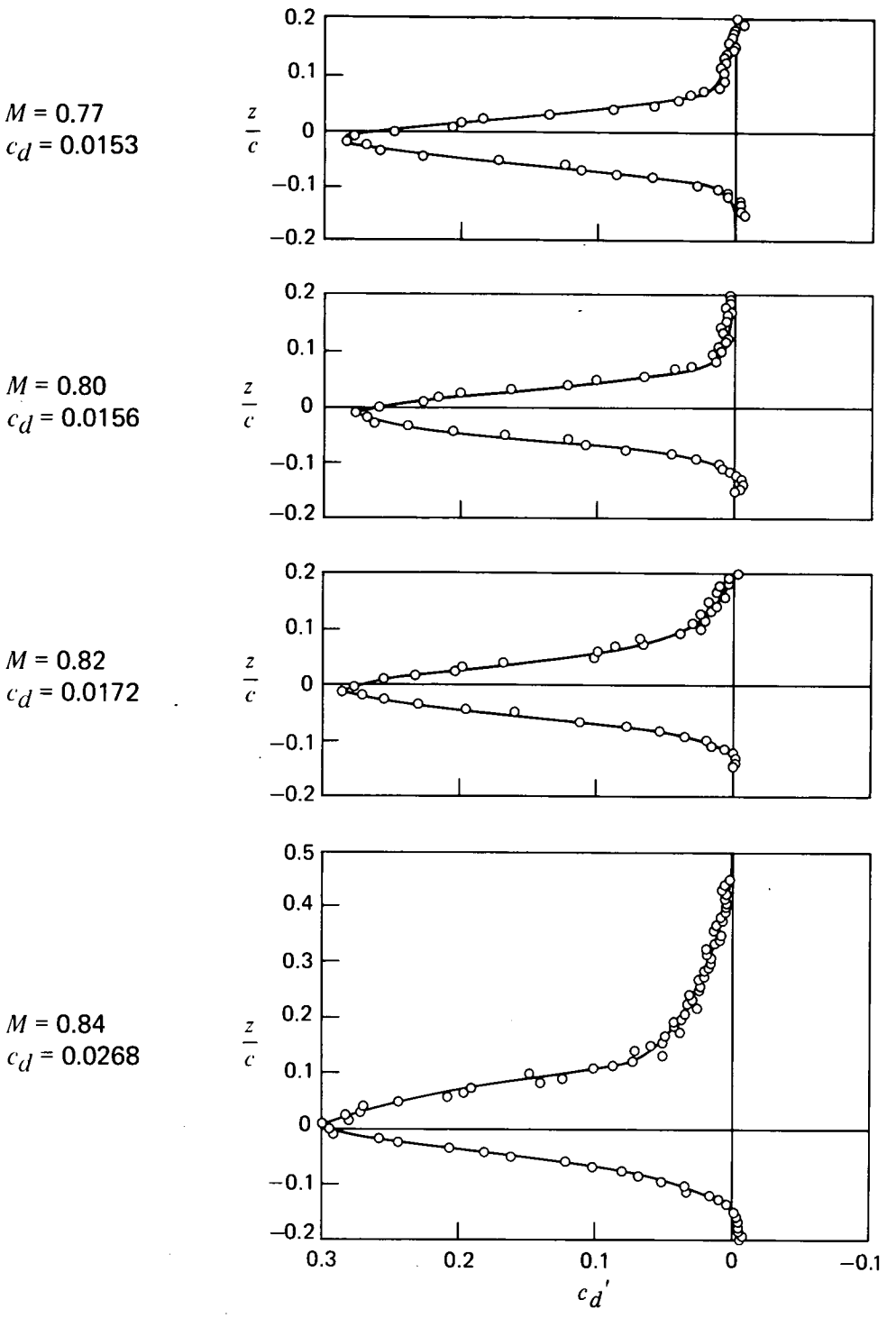

Figure 9.– Momentum defect profiles from drag rake 1.75 chord lengths downstream of trailing edge, $c_l = 0.53 \pm 0.02$, $Re_c = 3.0 \times 10^6$.

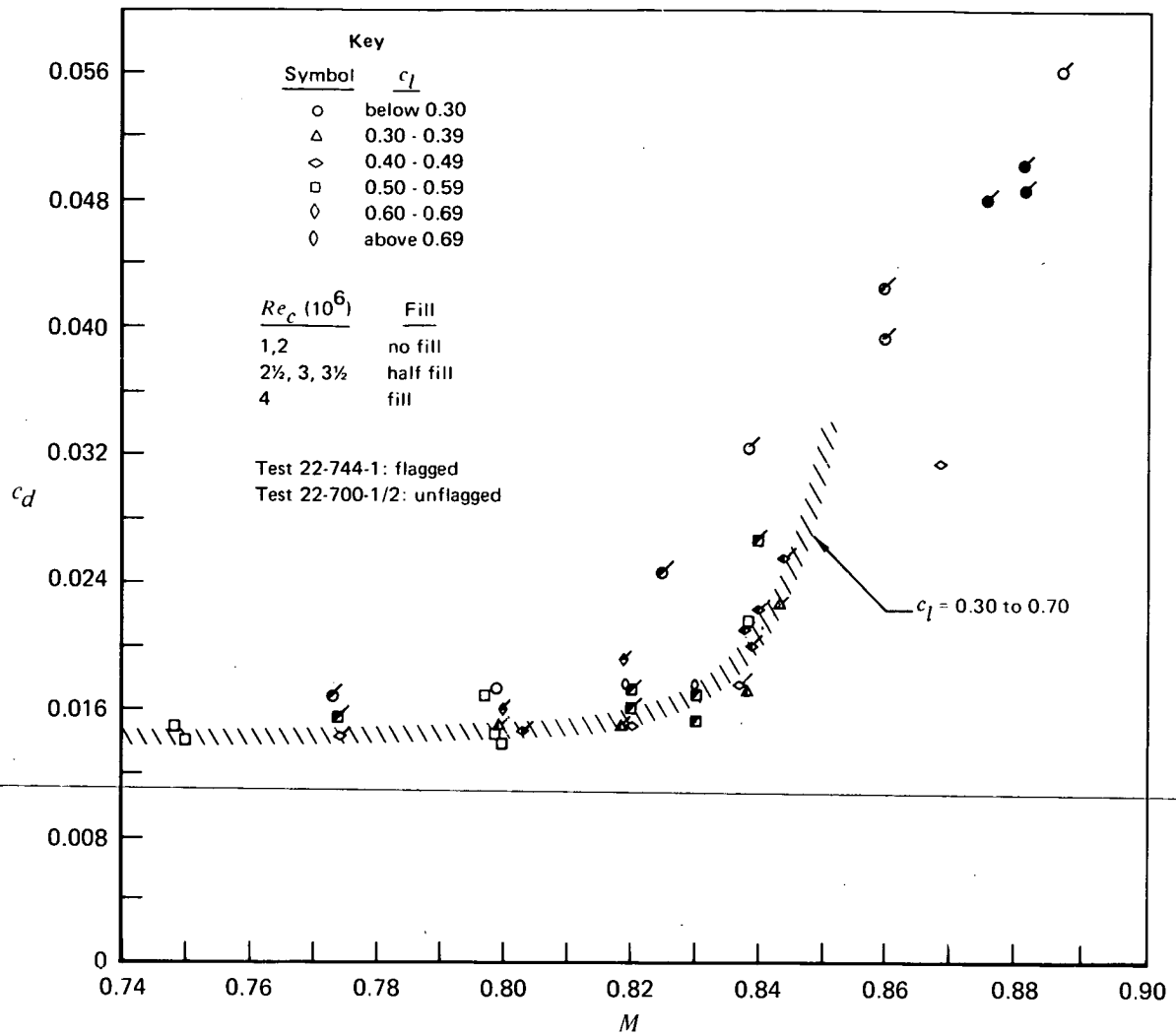

Figure 10.– Drag data.

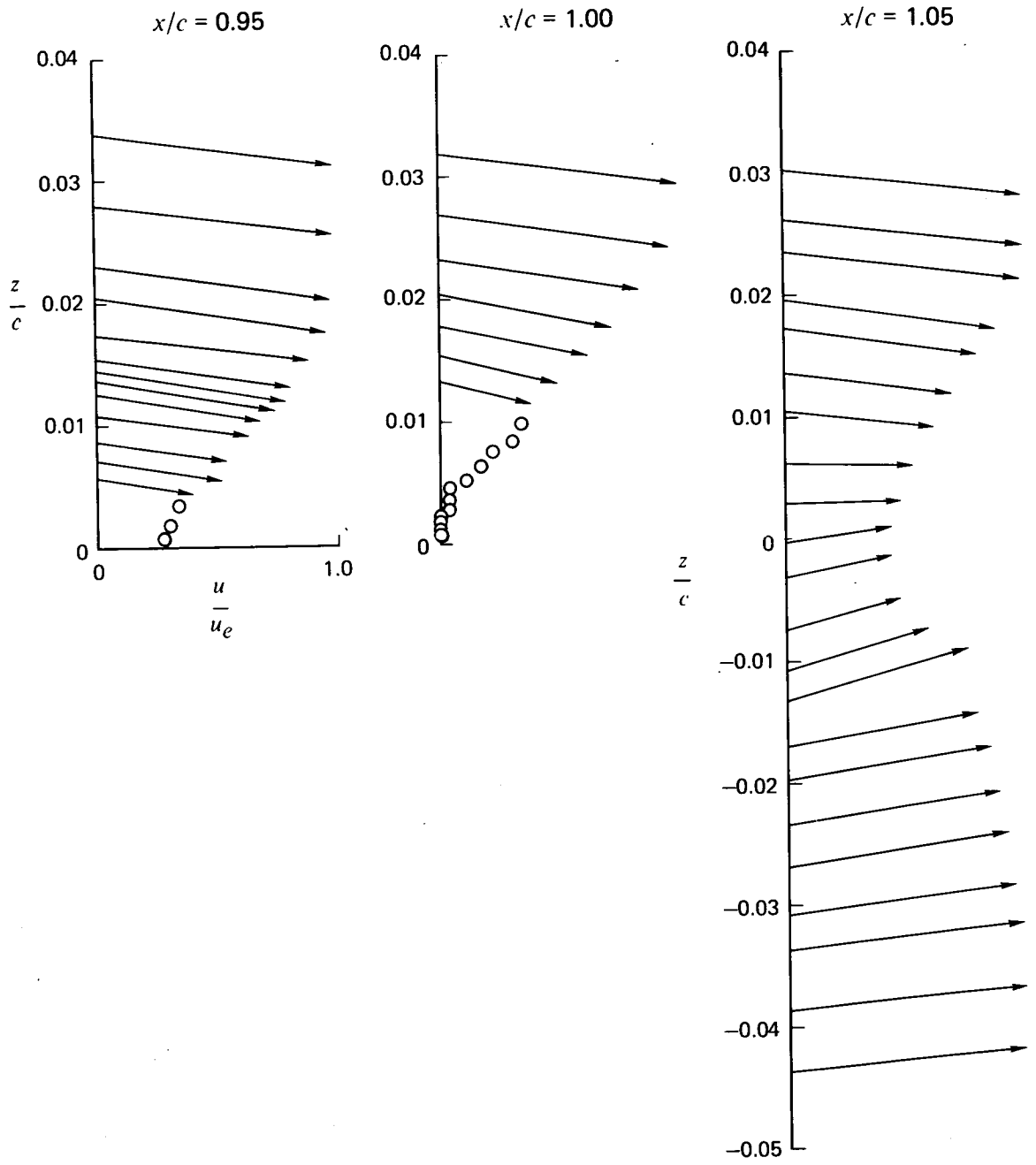

Figure 11.– Velocity profiles near trailing edge, $M = 0.83$, $c_l = 0.54$, $Re_c = 3.0 \times 10^6$.

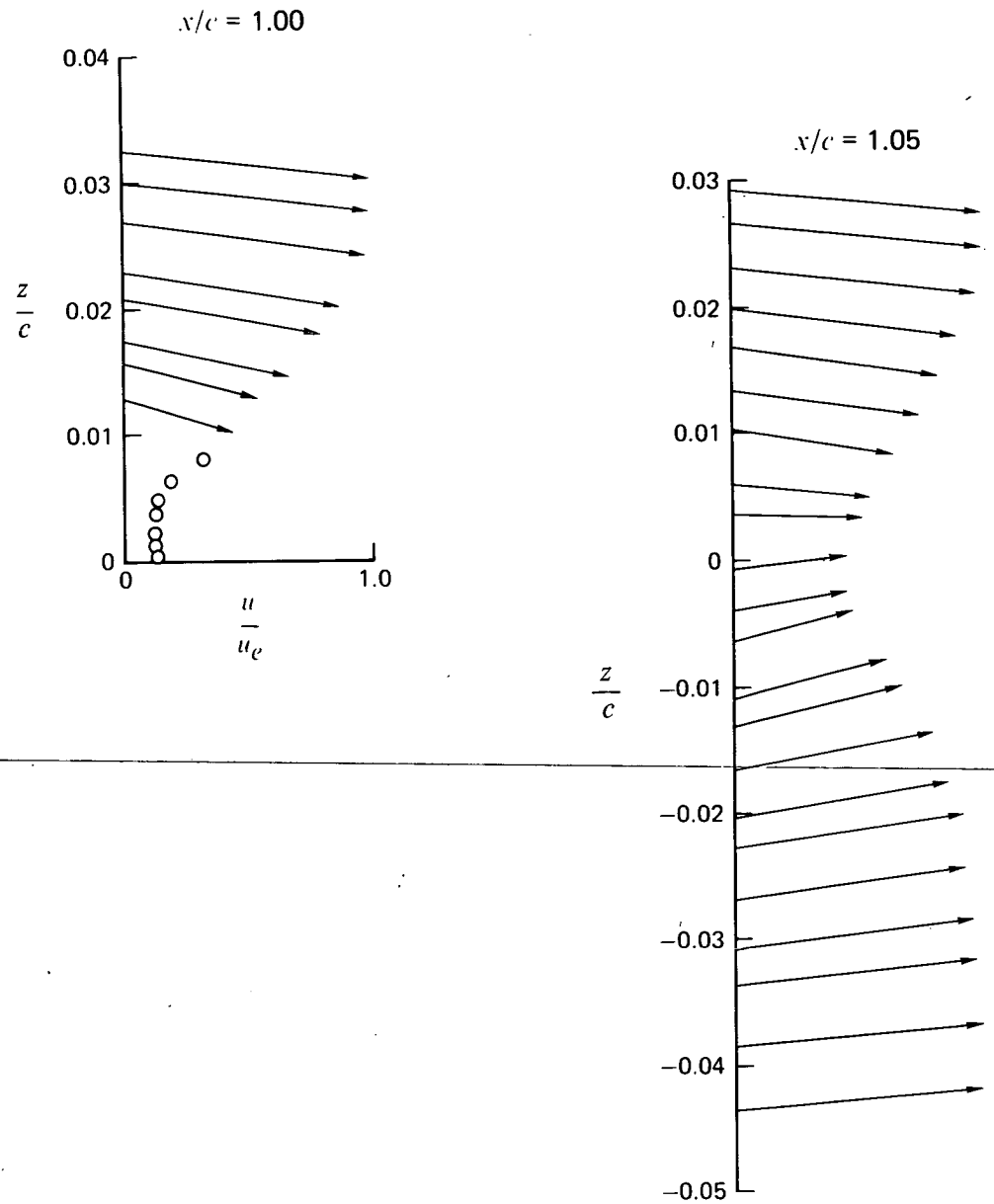

(a) $M = 0.82$

Figure 12.– Influence of Mach number on trailing edge and near-wake velocity profiles, $c_l = 0.56 \pm 0.03$, $Re_c = 3.0 \times 10^6$.

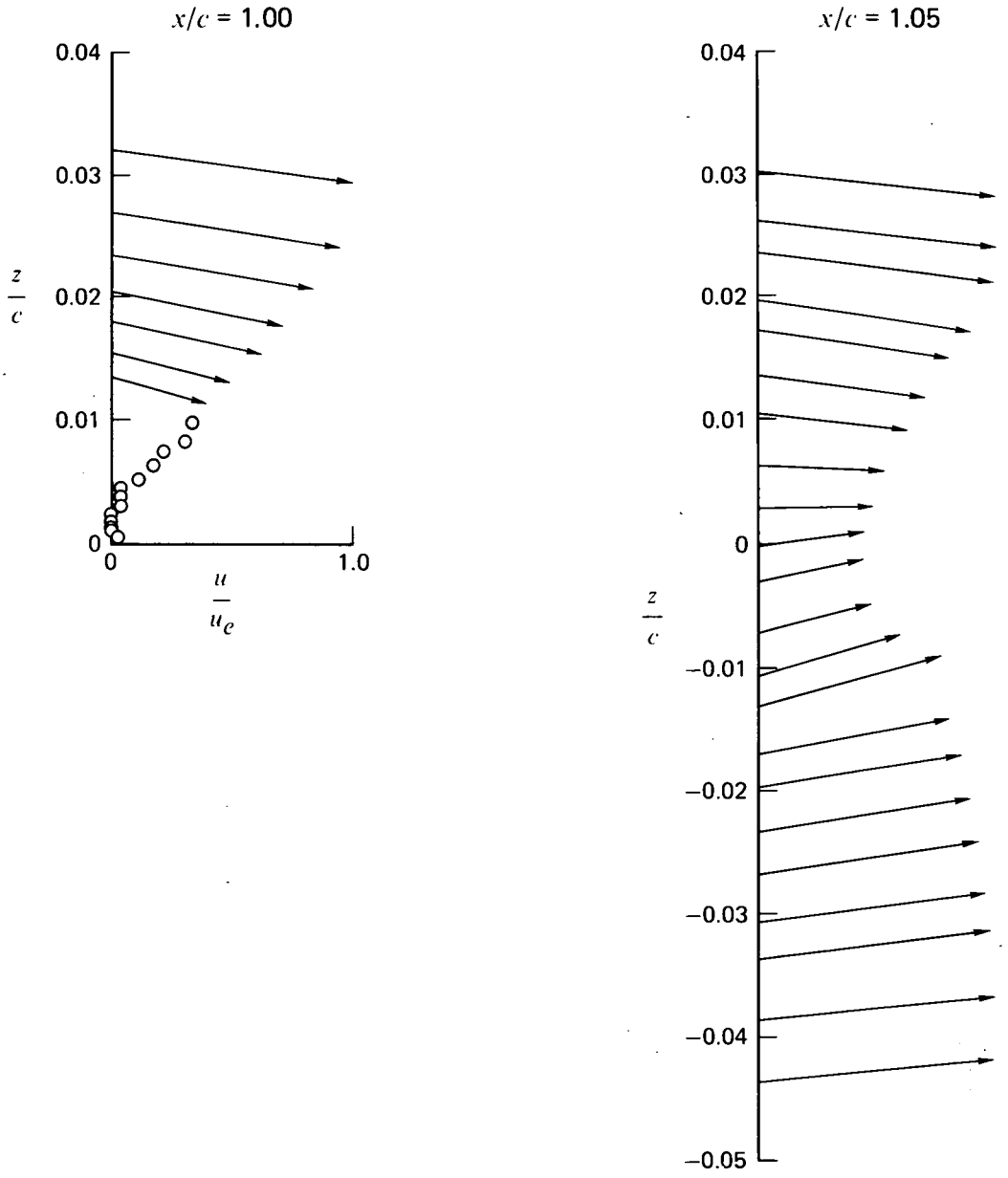

(b) $M = 0.83$

Figure 12.– Continued.

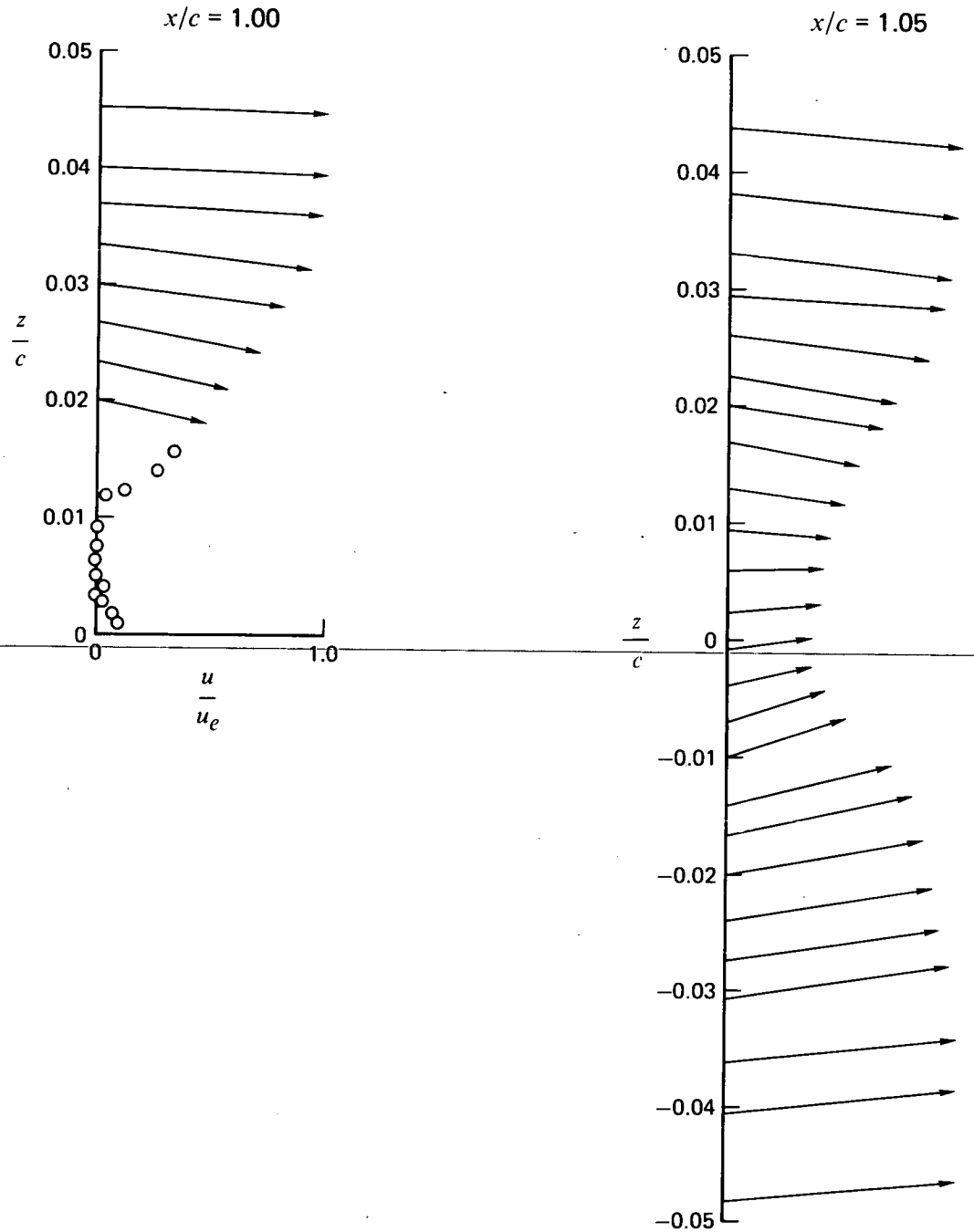

(c) $M = 0.84$

Figure 12.– Concluded.

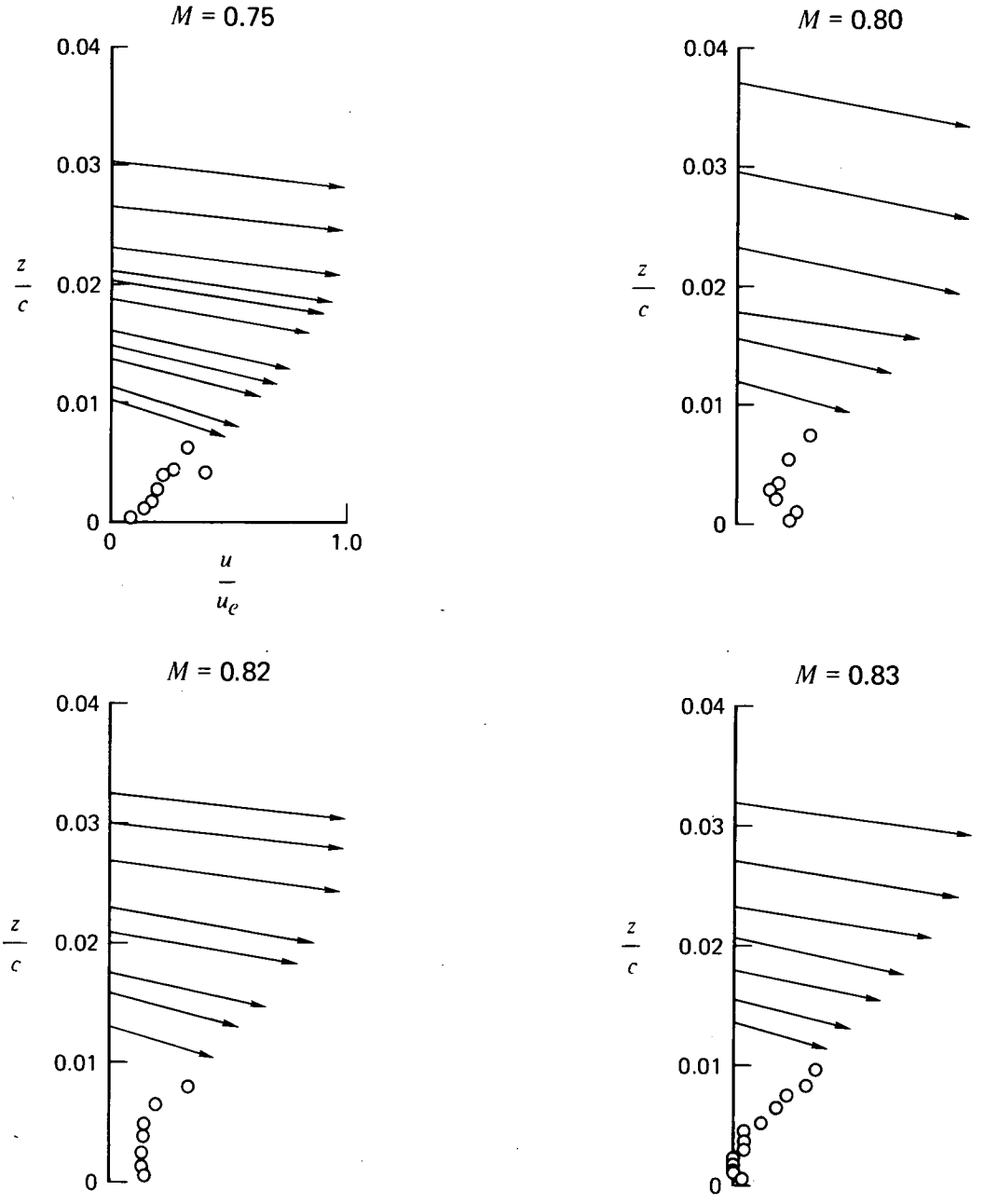

(a) $M = 0.75$; 0.80; 0.82; and 0.83

Figure 13.– Influence of Mach number on trailing edge velocity profiles, $c_l = 0.54 \pm 0.04$, $Re_c = 3.0 \times 10^6$.

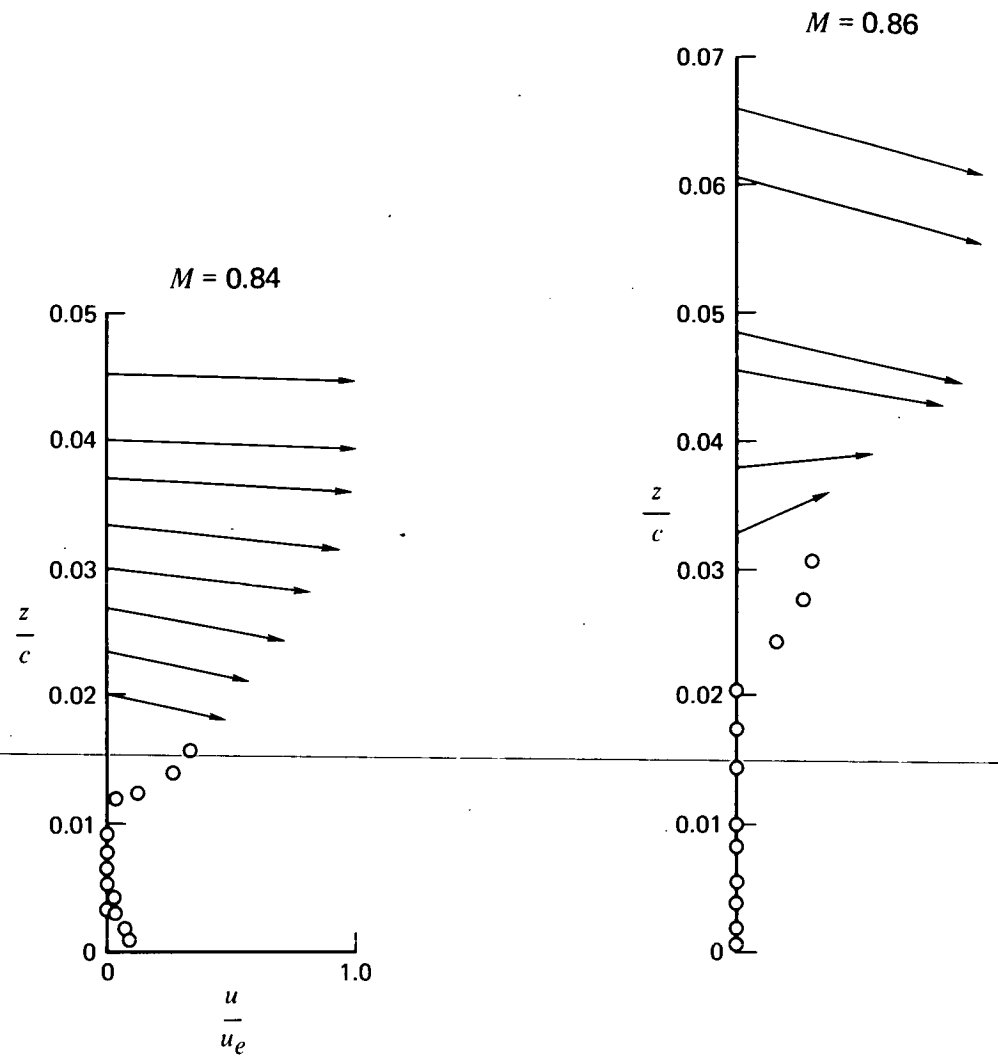

(b) $M = 0.84$ and 0.86

Figure 13.– Concluded.

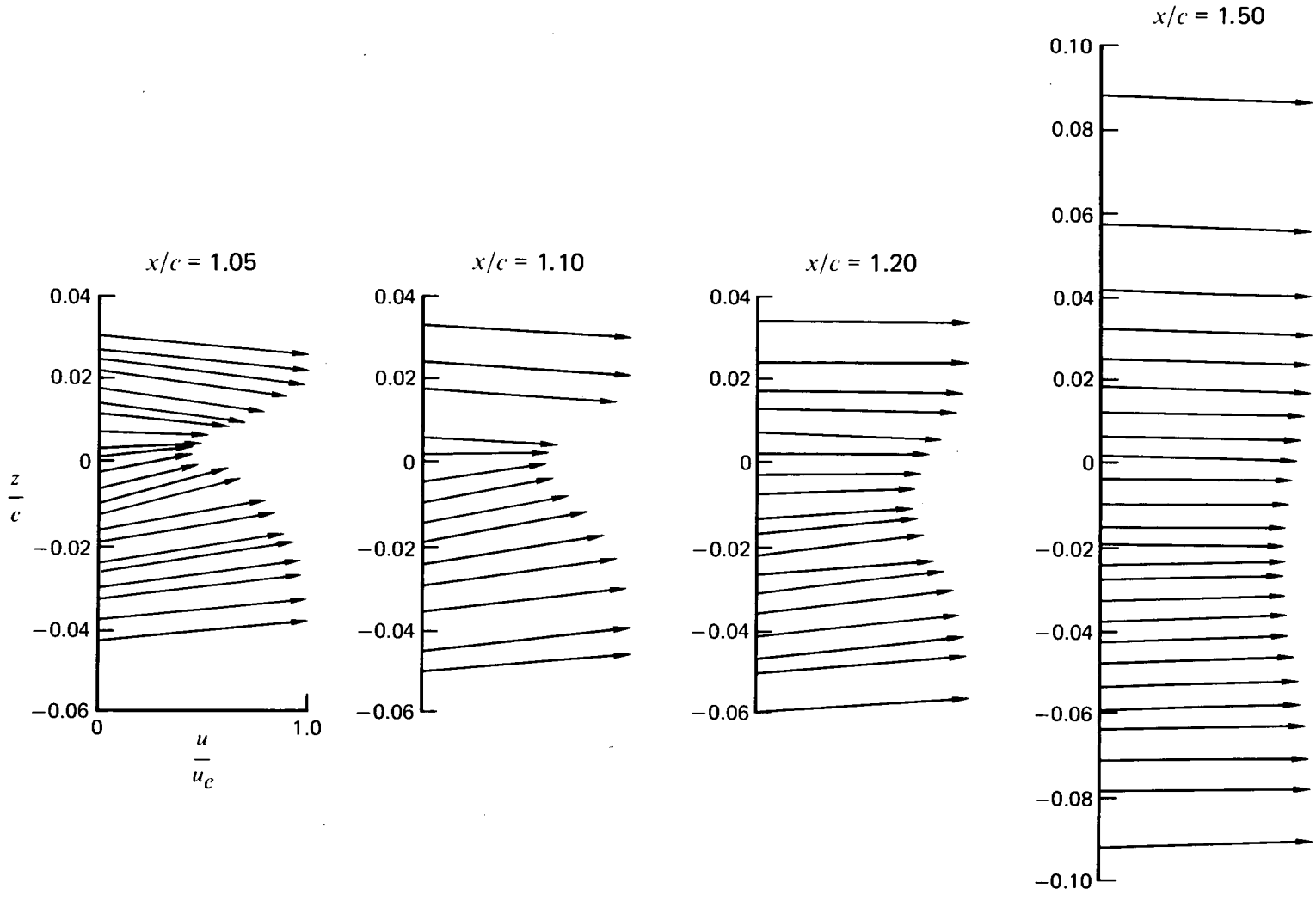

Figure 14.– Evolution of near-wake velocity profiles, $M = 0.83$, $c_l = 0.54$, $Re_c = 3.0 \times 10^6$.

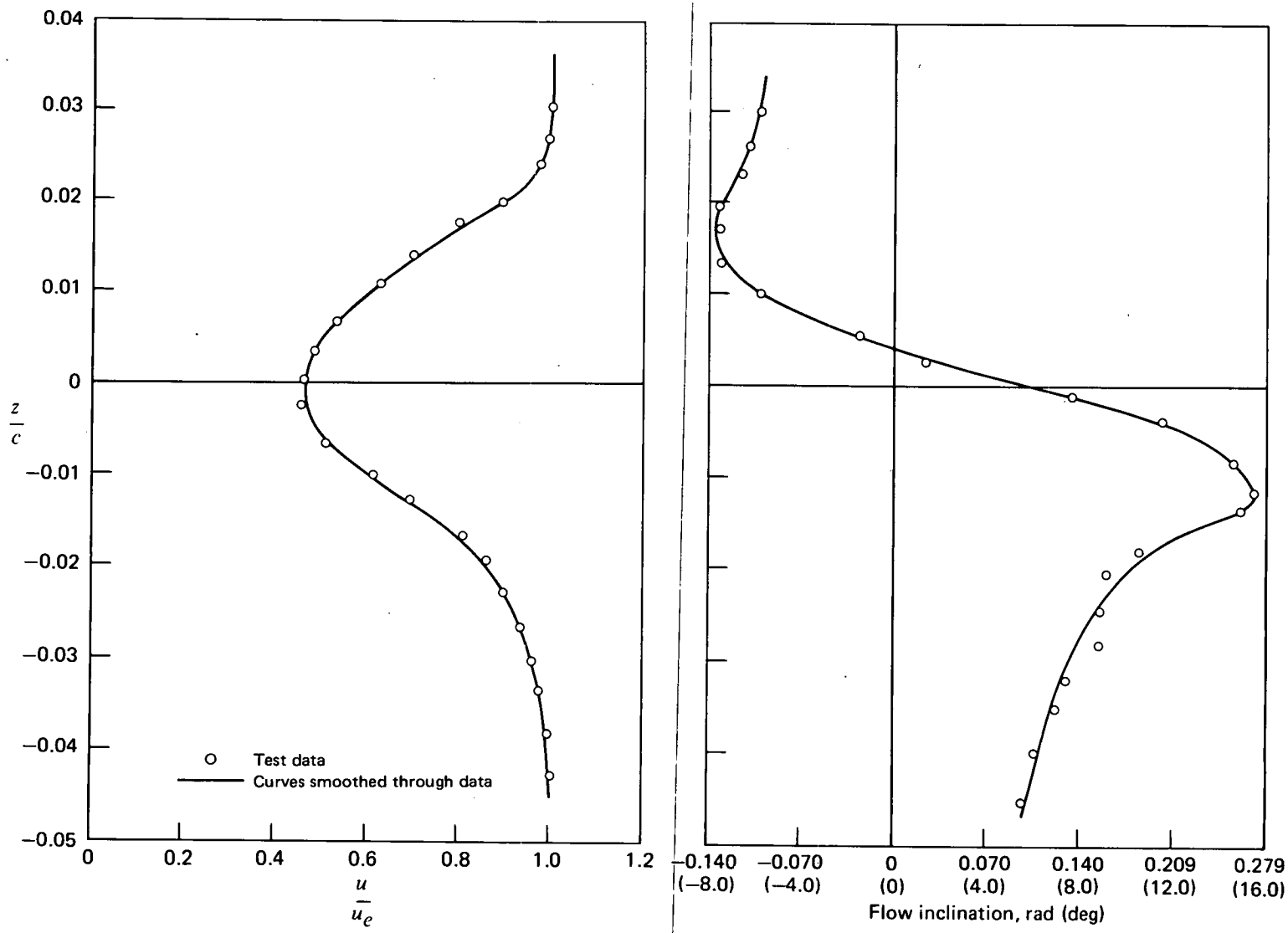

Figure 15.– Near-wake speed and flow inclination profiles, $x/c = 1.05$, $M = 0.83$, $c_l = 0.54$, $Re_c = 3.0 \times 10^6$.

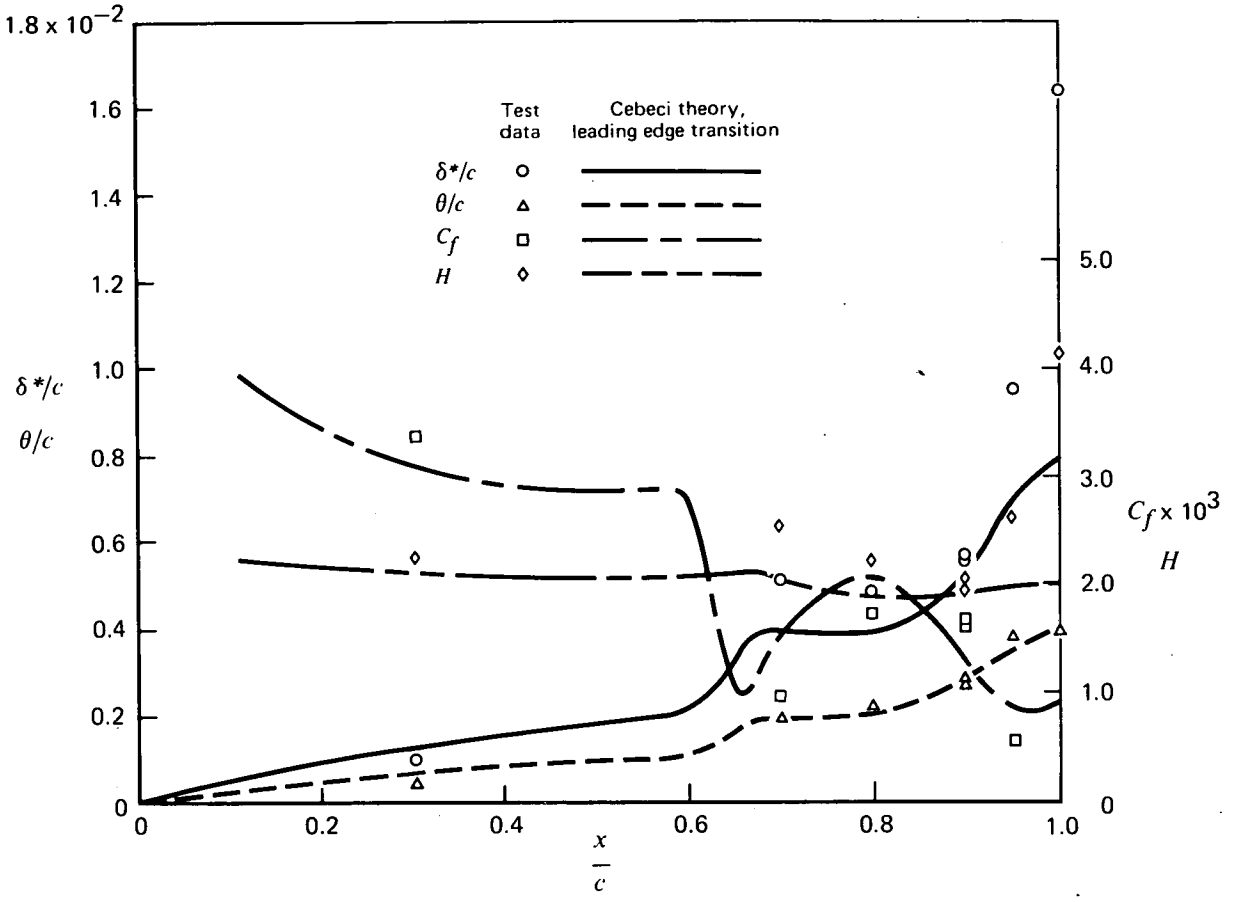

Figure 16.– Comparison of measured and calculated boundary layer properties, $M = 0.83, c_l = 0.54, Re_c = 3.0 \times 10^6$.

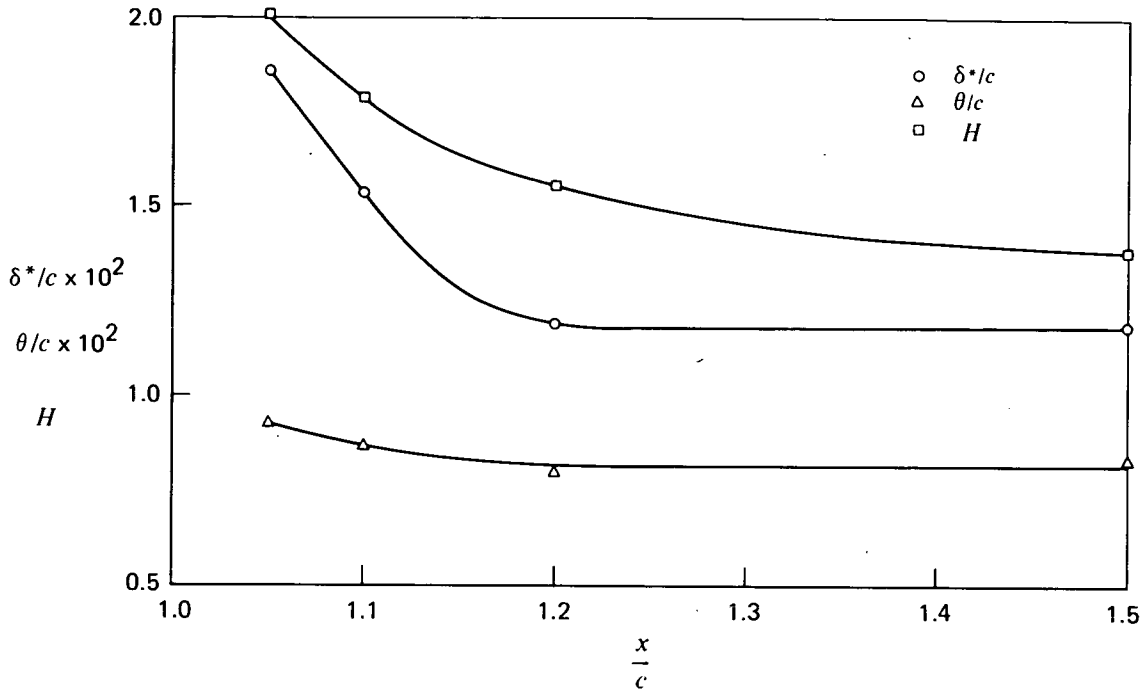

Figure 17.— Near-wake integral properties, $M = 0.83$, $c_l = 0.54$, $Re_c = 3.0 \times 10^6$.

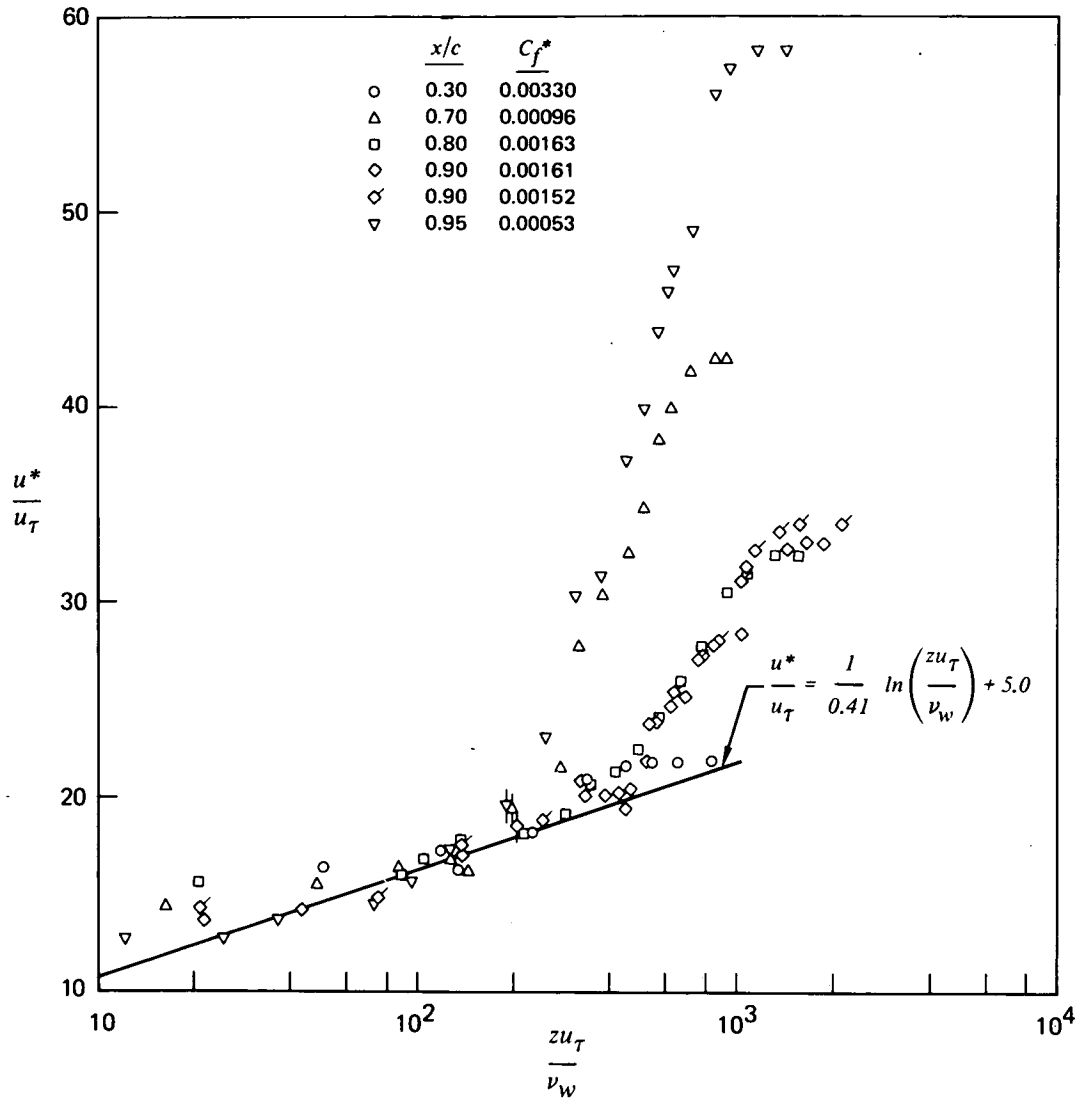

Figure 18.– Transformed boundary layer profiles in law-of-the-wall coordinates, $M = 0.83, c_l = 0.54, Re_c = 3.0 \times 10^6$.

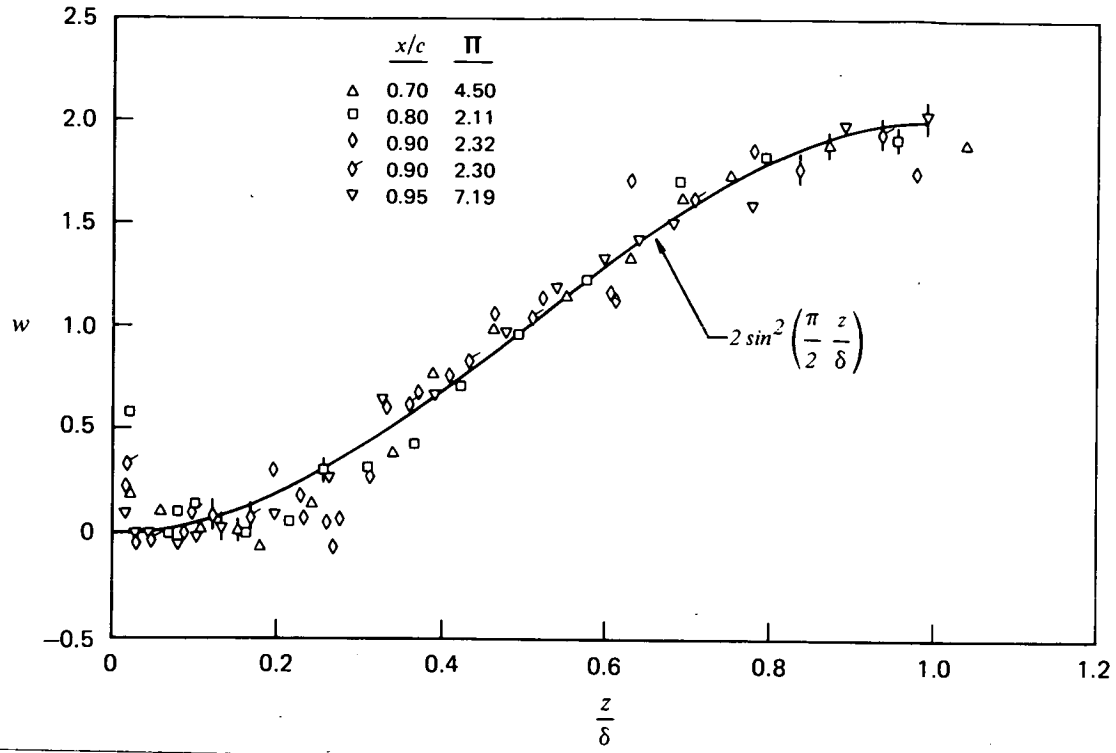

Figure 19.– Wake components of transformed boundary layer profiles, $M = 0.83$, $c_l = 0.54$, $Re_c = 3.0 \times 10^6$.

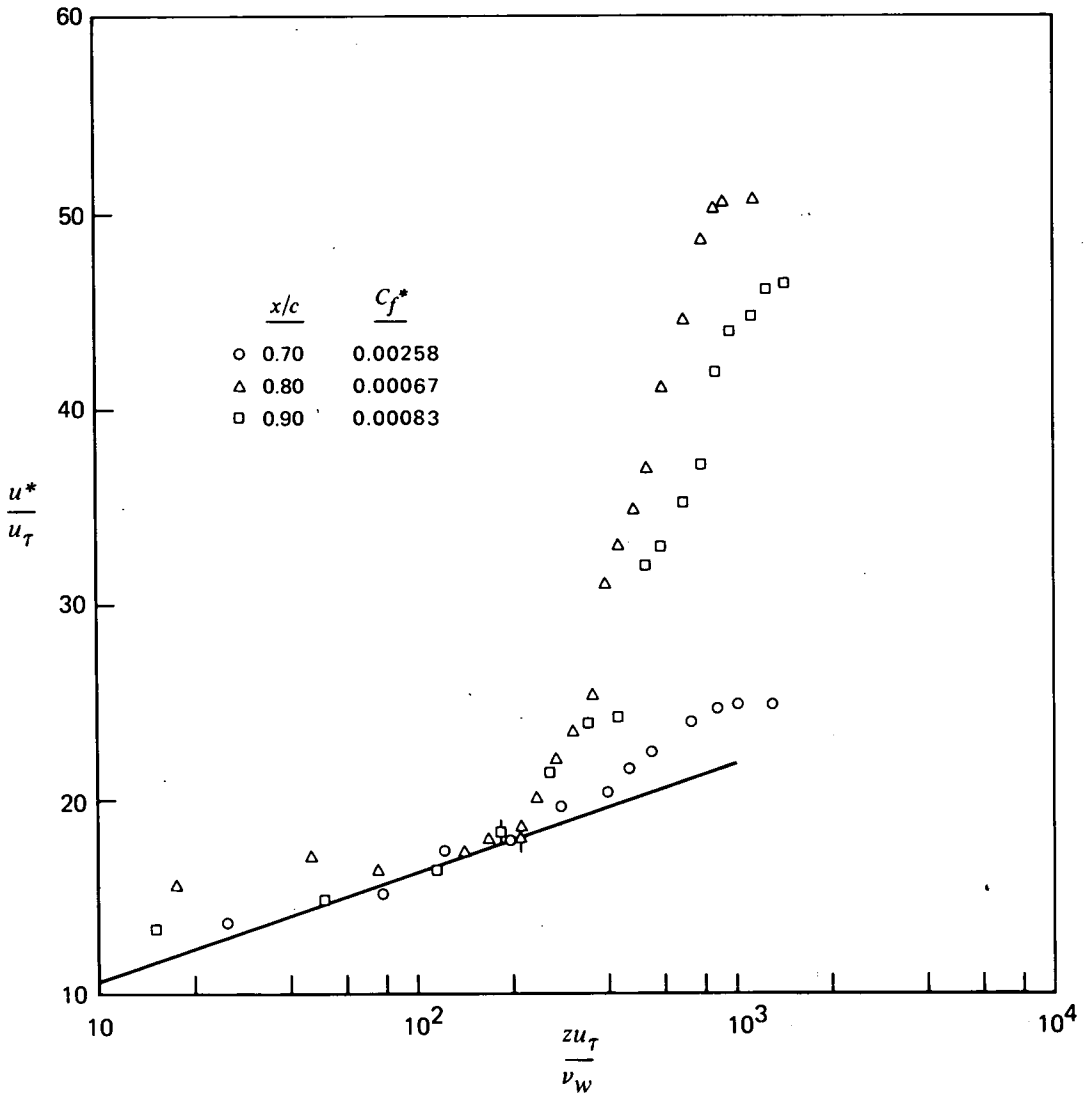

Figure 20.– Transformed boundary layer profiles in law-of-the-wall coordinates, $M = 0.84$, $c_l = 0.58$, $Re_c = 3.0 \times 10^6$.

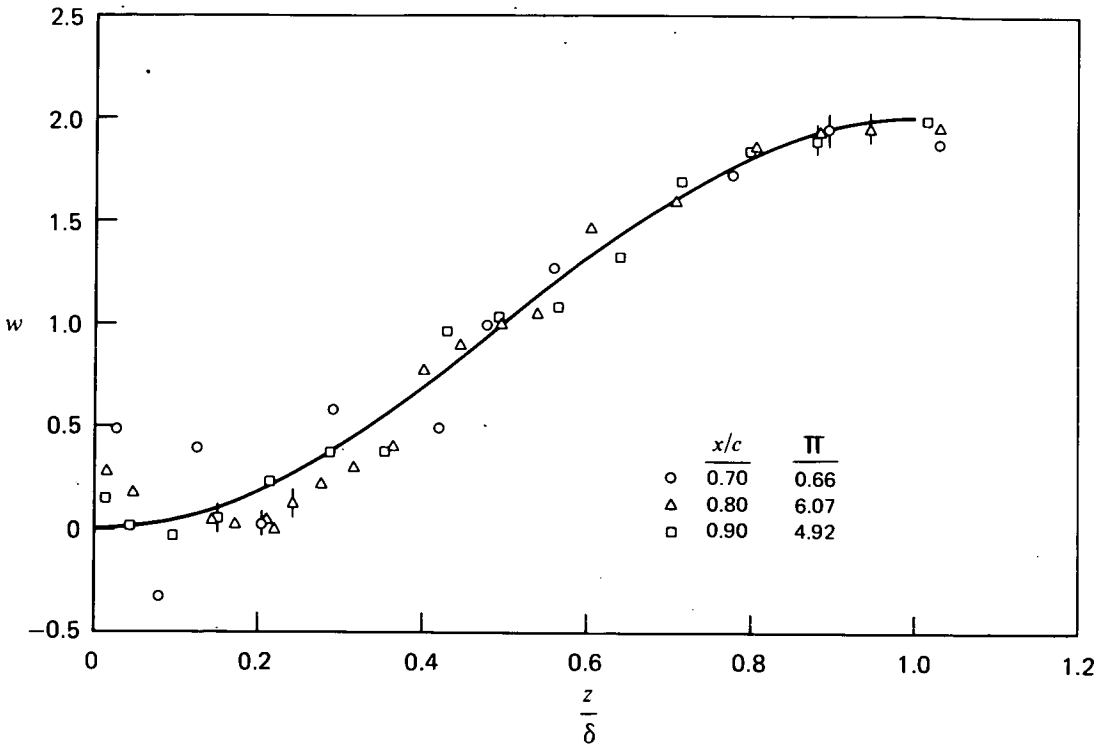

Figure 21.– Wake components of transformed boundary layer profiles, $M = 0.84$, $c_l = 0.58$, $Re_c = 3.0 \times 10^6$.

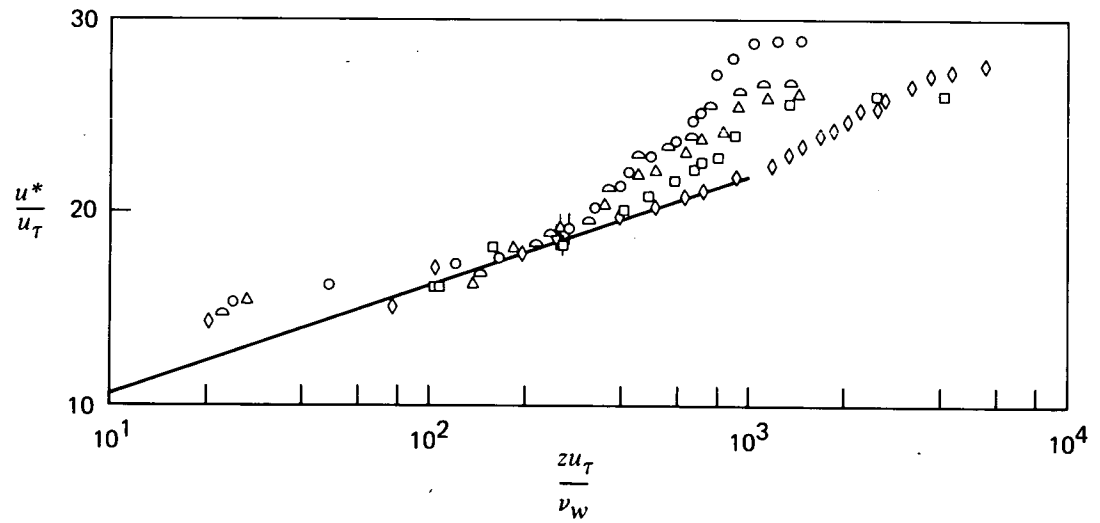

	M	Re_c	c_l	C_f^*
⌓	0.86	3.0×10^6	0.48	0.00216
○	0.82	3.0×10^6	0.53	0.00203
△	0.80	3.0×10^6	0.53	0.00249
□	0.75	3.0×10^6	0.51	0.00258
◇	0.60	2.0×10^6	0.90	0.00240

Figure 22.– Transformed boundary layer profiles in law-of-the-wall coordinates, $x/c = 0.70$.

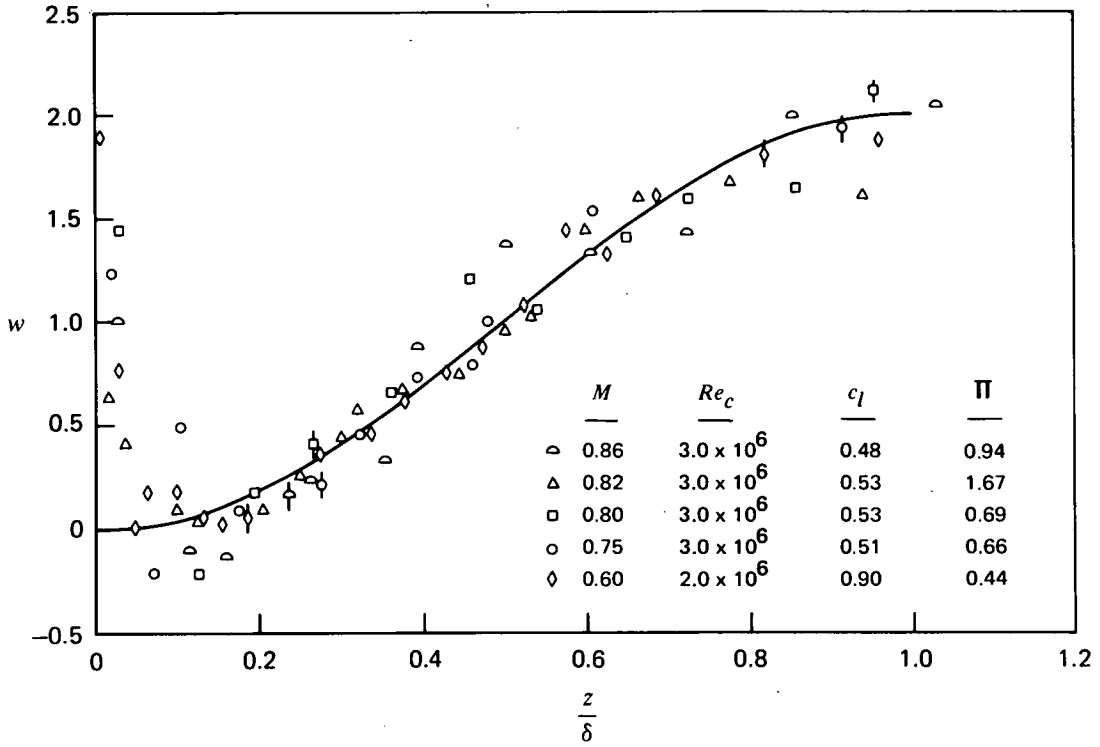

Figure 23.– Wake components of transformed boundary layer profiles, $x/c = 0.70$.

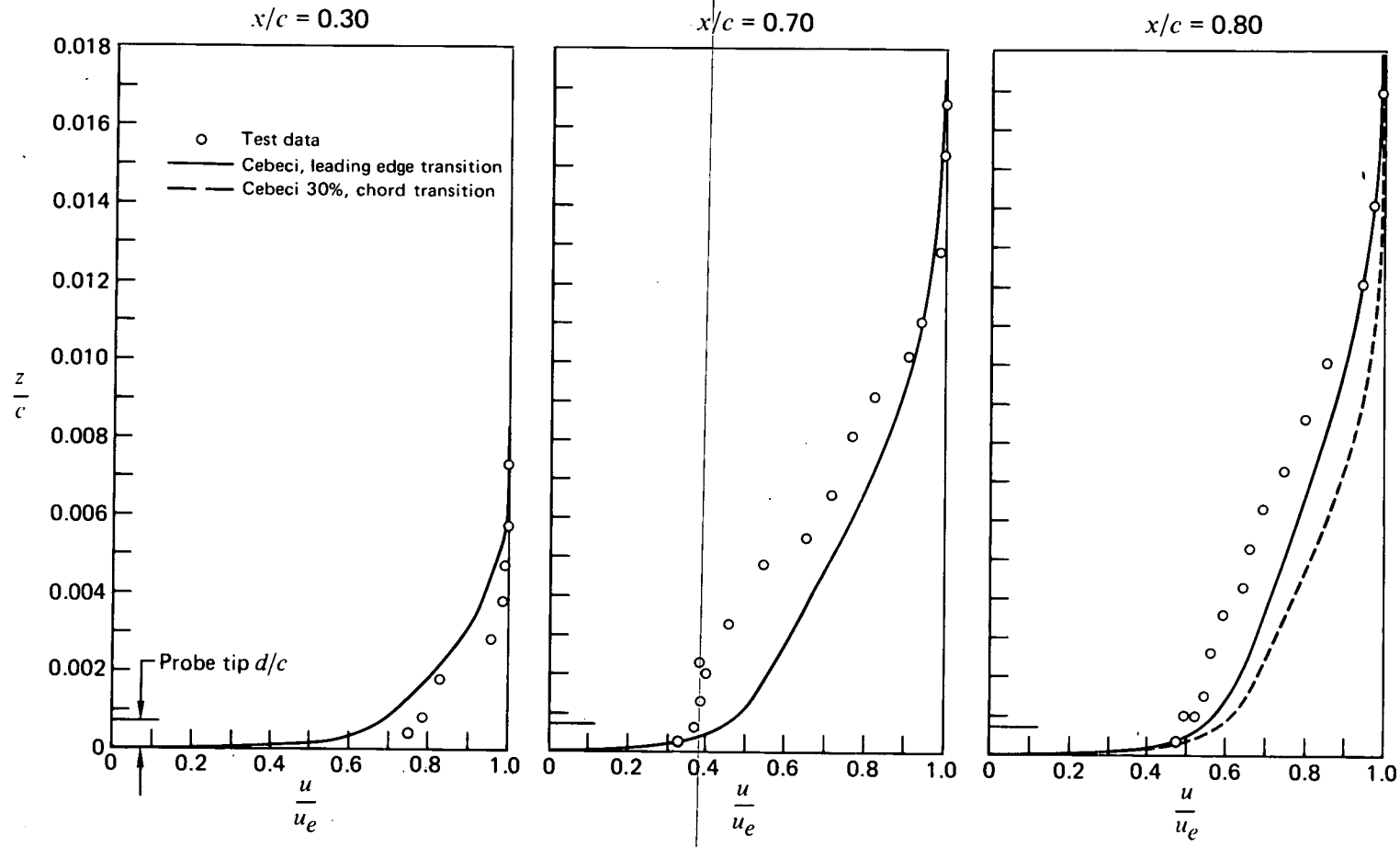

(a) x/c = 0.30; 0.70; and 0.80.

Figure 24.– Boundary layer speed profile development; experiment versus Cebeci program calculation, $M = 0.83$, $c_l = 0.54$, $Re_c = 3.0 \times 10^6$.

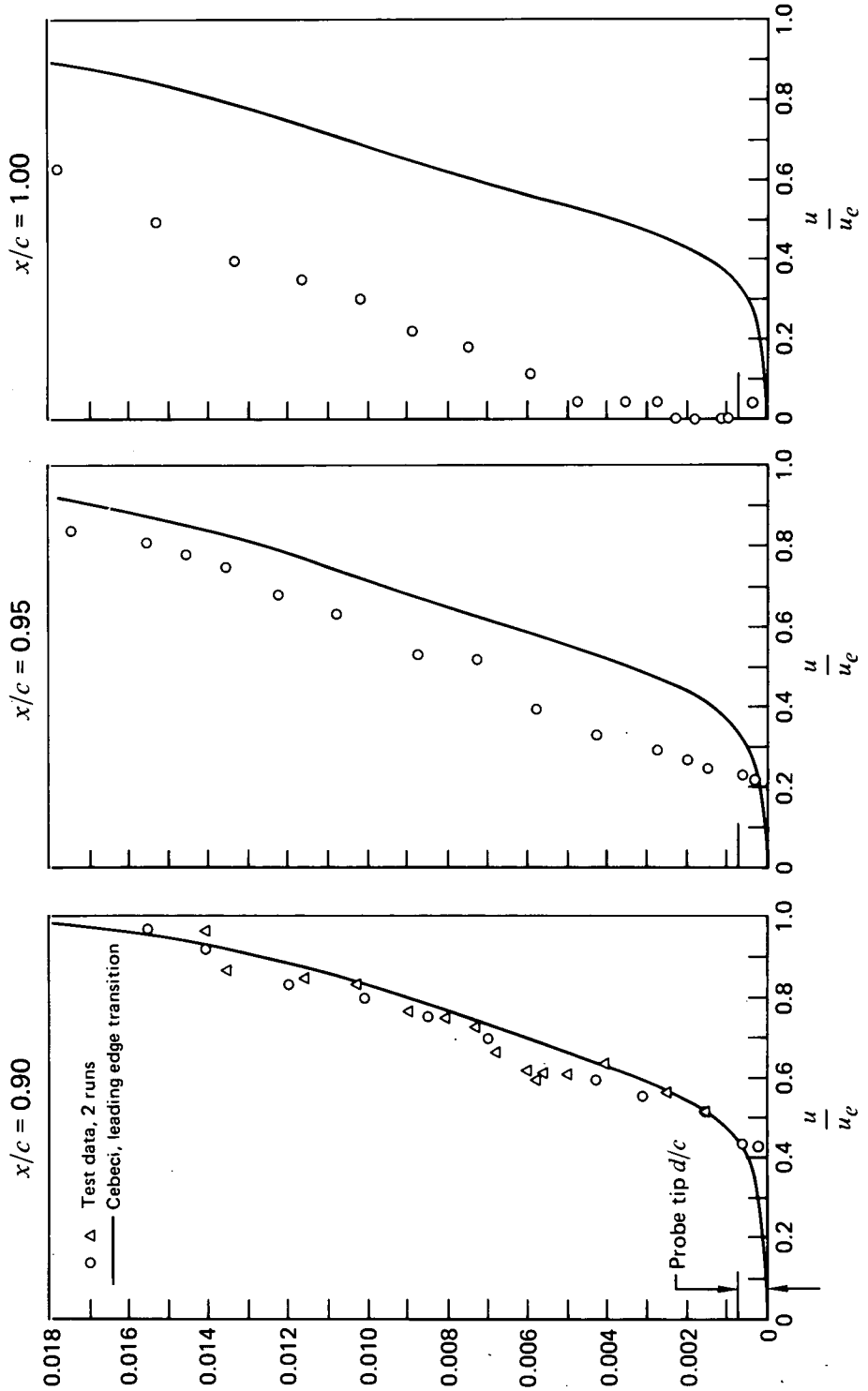

(b) $x/c = 0.90; 0.95;$ and 1.00

Figure 24.– Concluded.

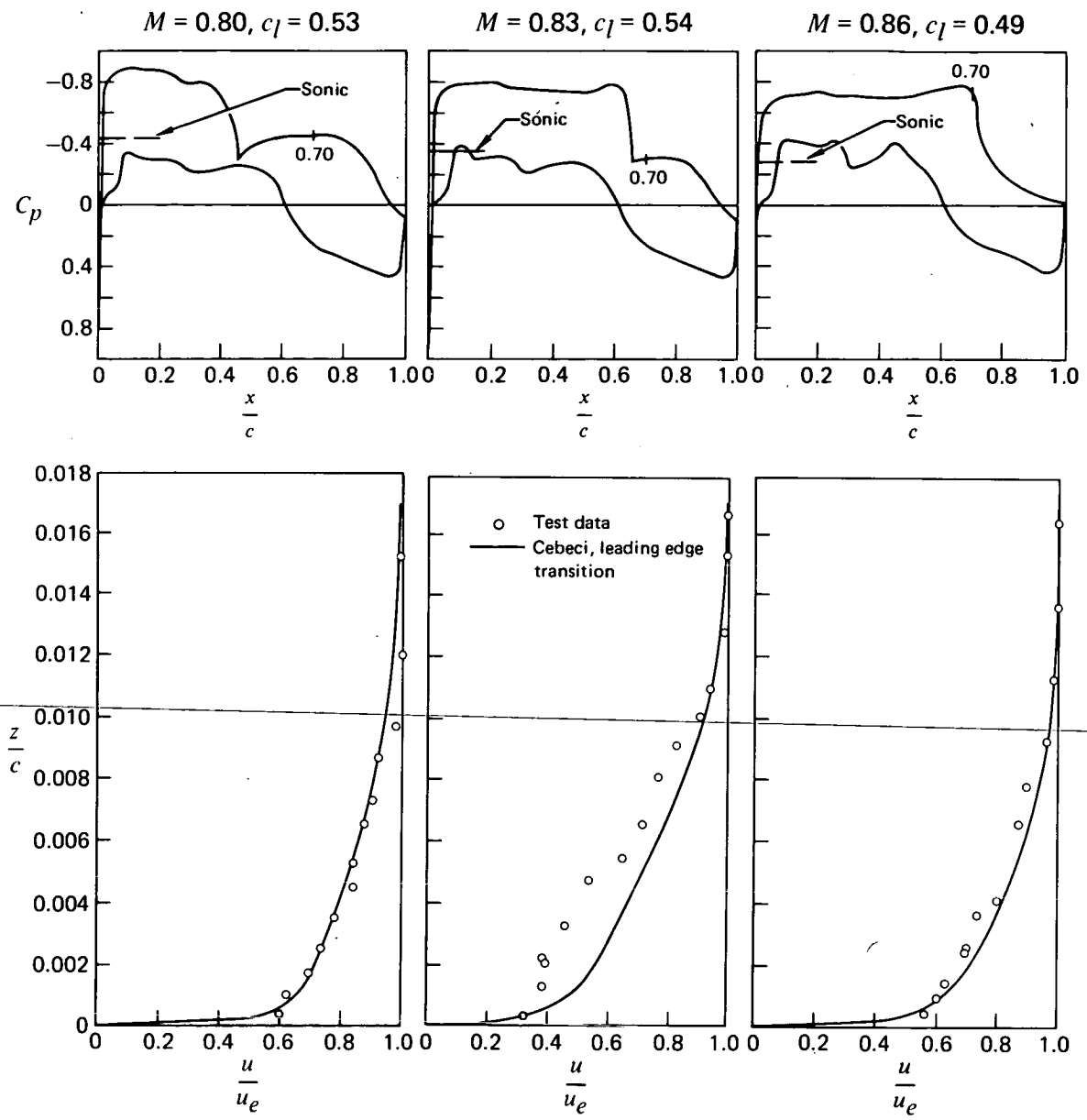

Figure 25.– Boundary layer speed profiles at $x/c = 0.70$ for different relative shock locations; experiment versus Cebeci program calculation, $Re_c = 3.0 \times 10^6$.

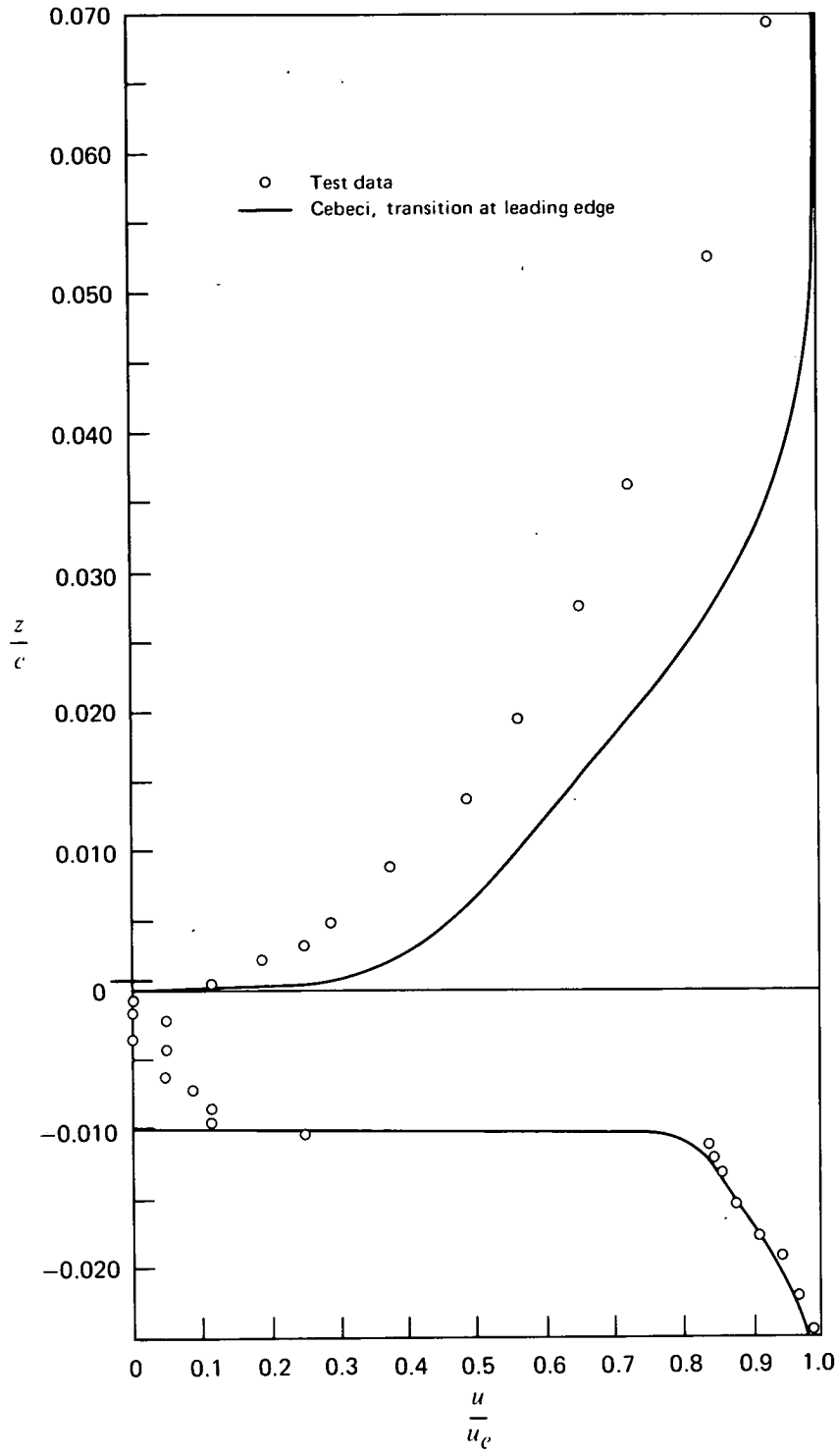

Figure 26.– Wake speed profile within $x/c = 0.001$ downstream of trailing edge, $M = 0.60$, $c_l = 0.91$, $Re_c = 2.0 \times 10^6$.

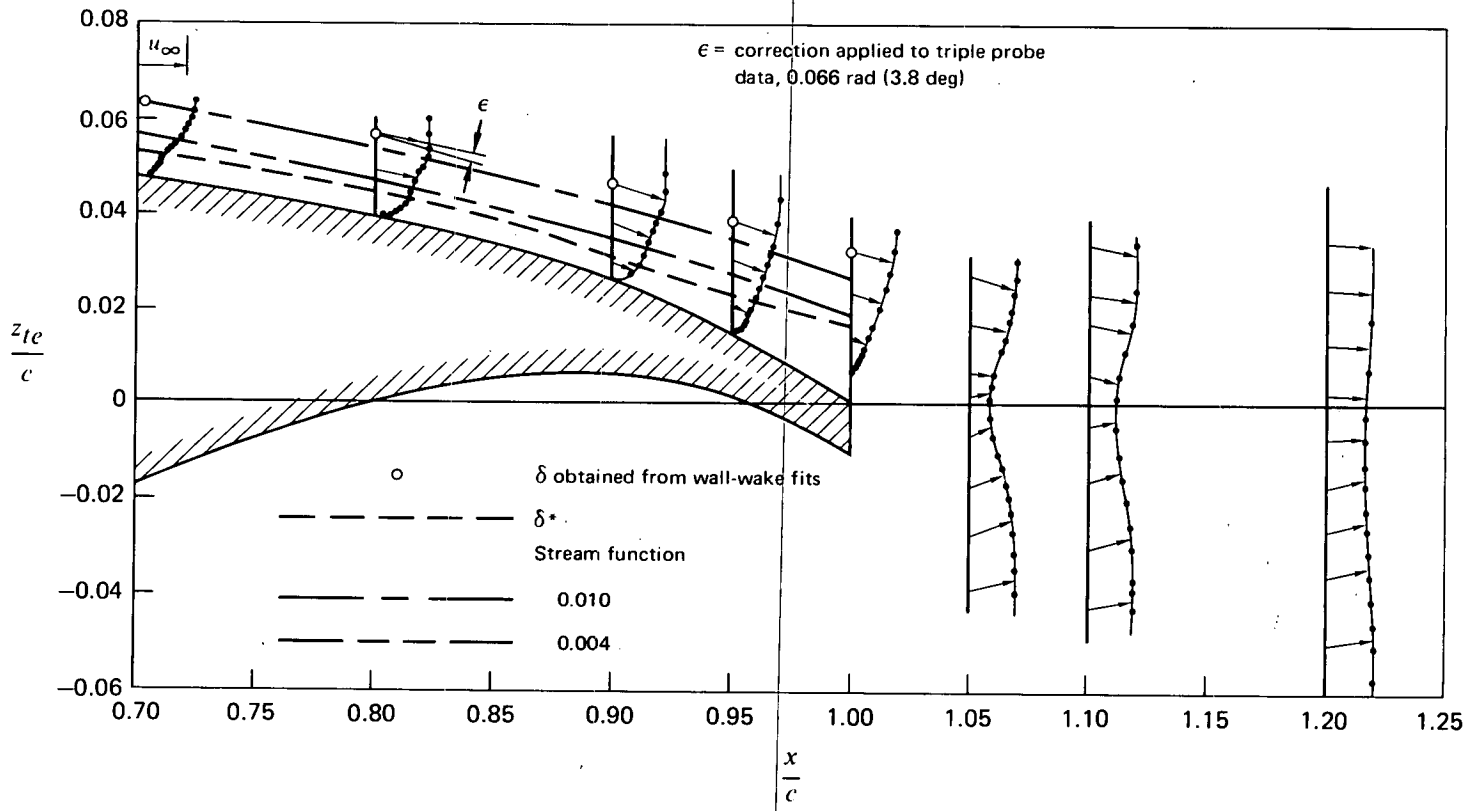

Figure 27.– Flow field details near trailing edge, $M = 0.83$, $c_l = 0.54$, $Re_c = 3.0 \times 10^6$.

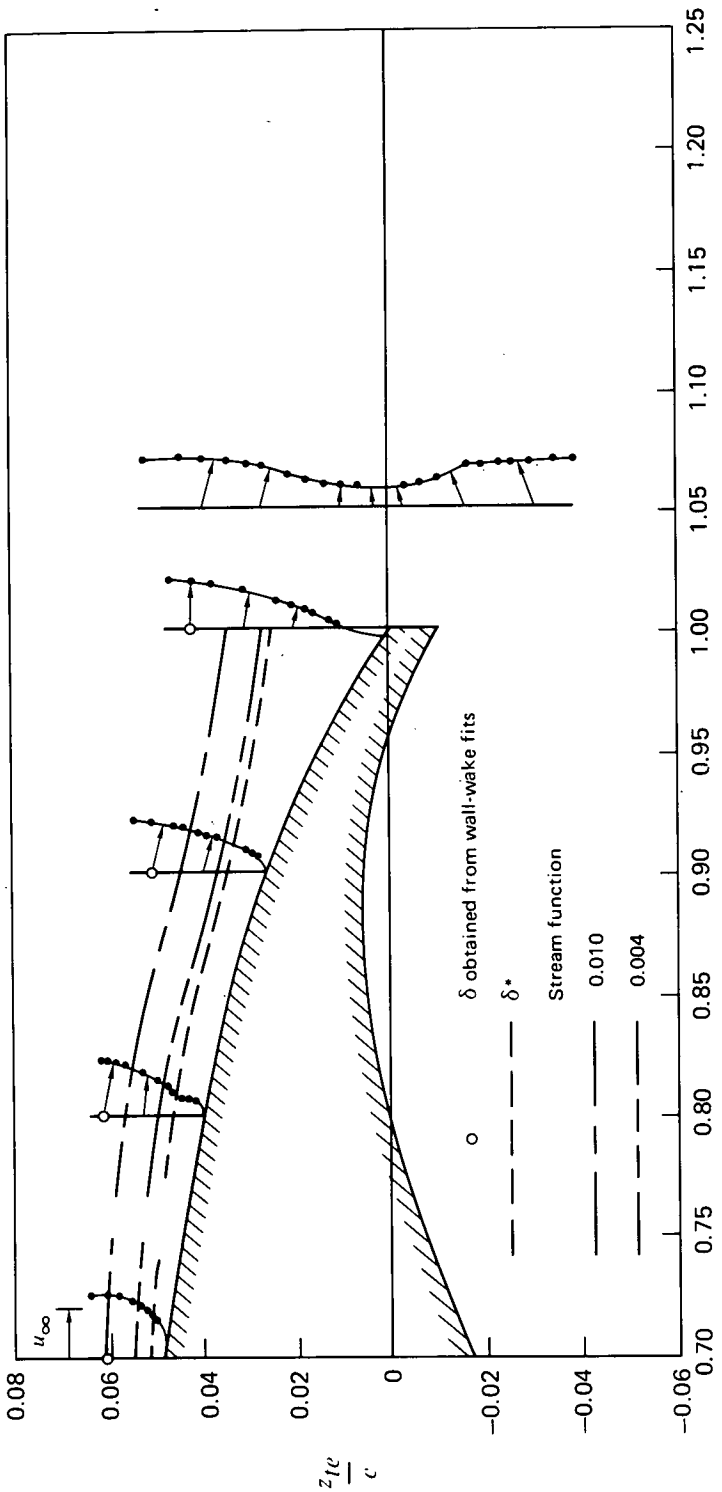

Figure 28.– Flow field details near trailing edge, $M = 0.84$, $c_j = 0.58$, $Re_c = 3.0 \times 10^6$.

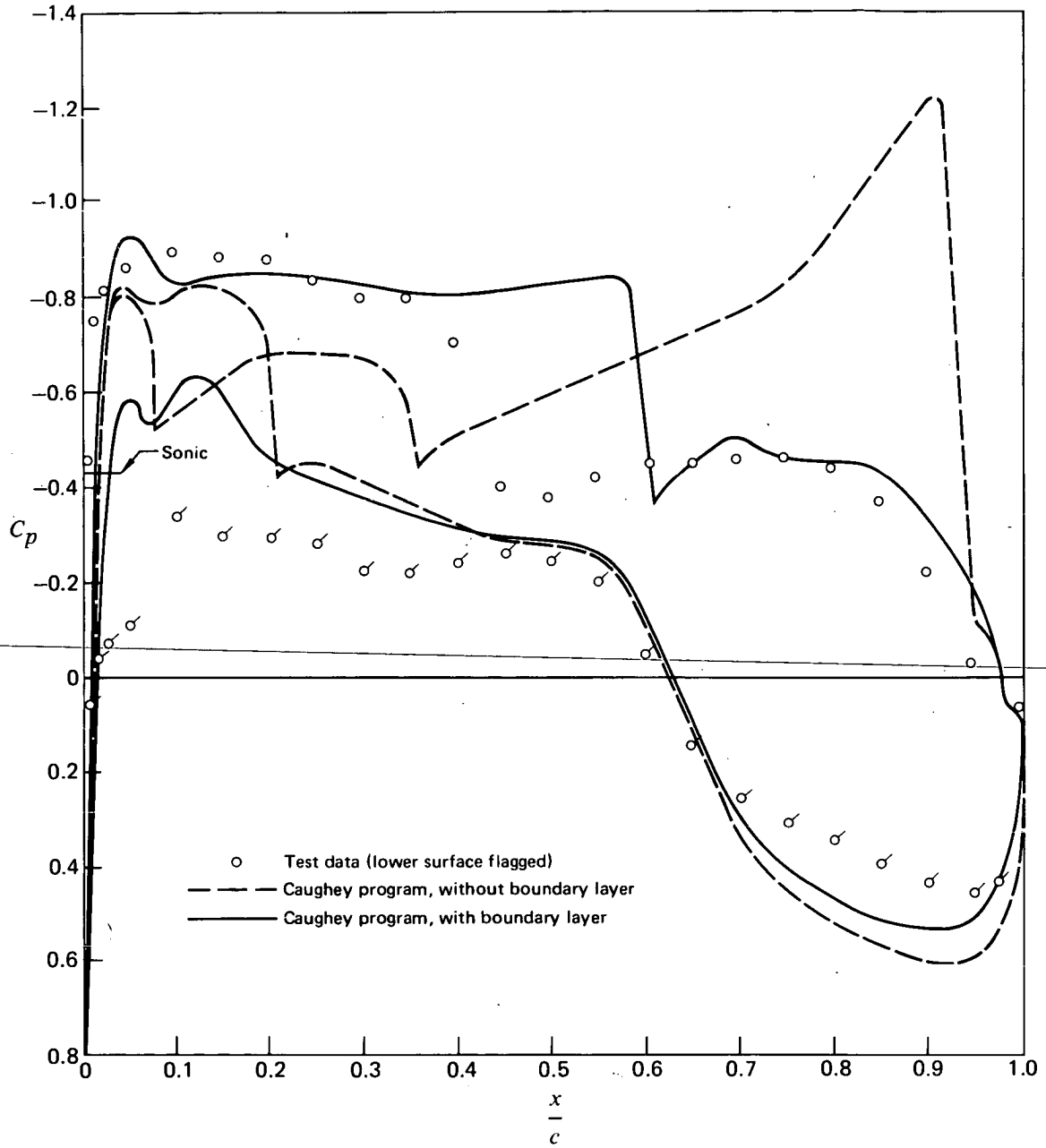

Figure 29.– Comparison between computed and measured pressure distributions, $M = 0.80$, $c_l = 0.54 \pm 0.01$, $Re_c = 3.0 \times 10^6$.

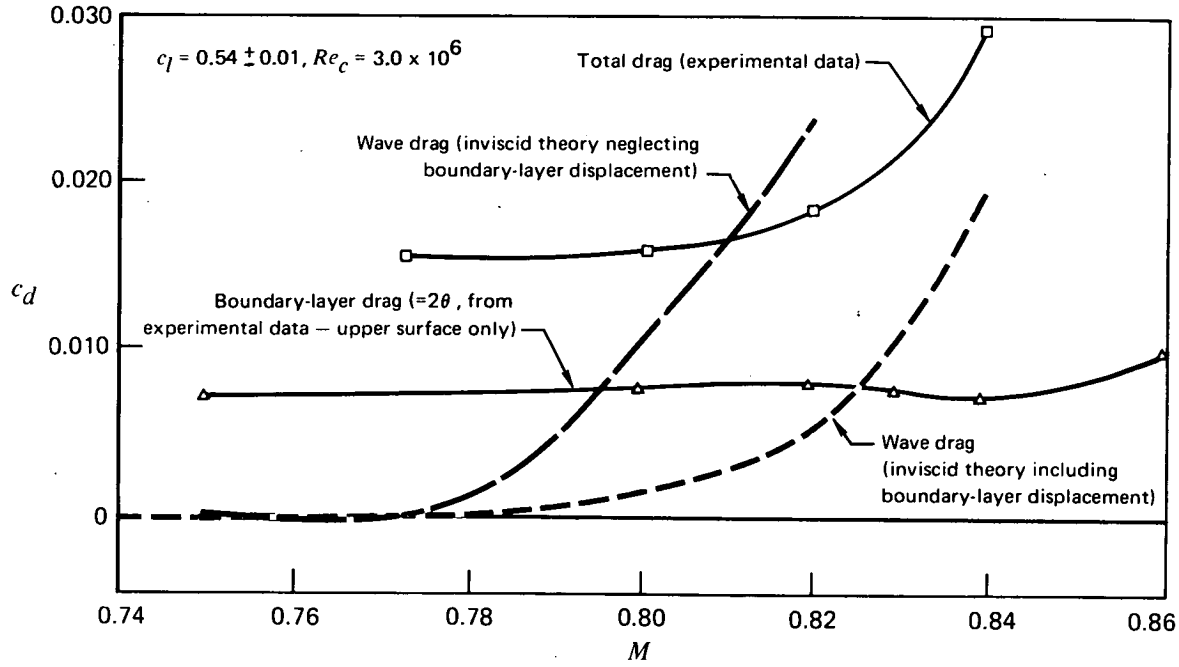

Figure 30.– Drag-rise characteristics.

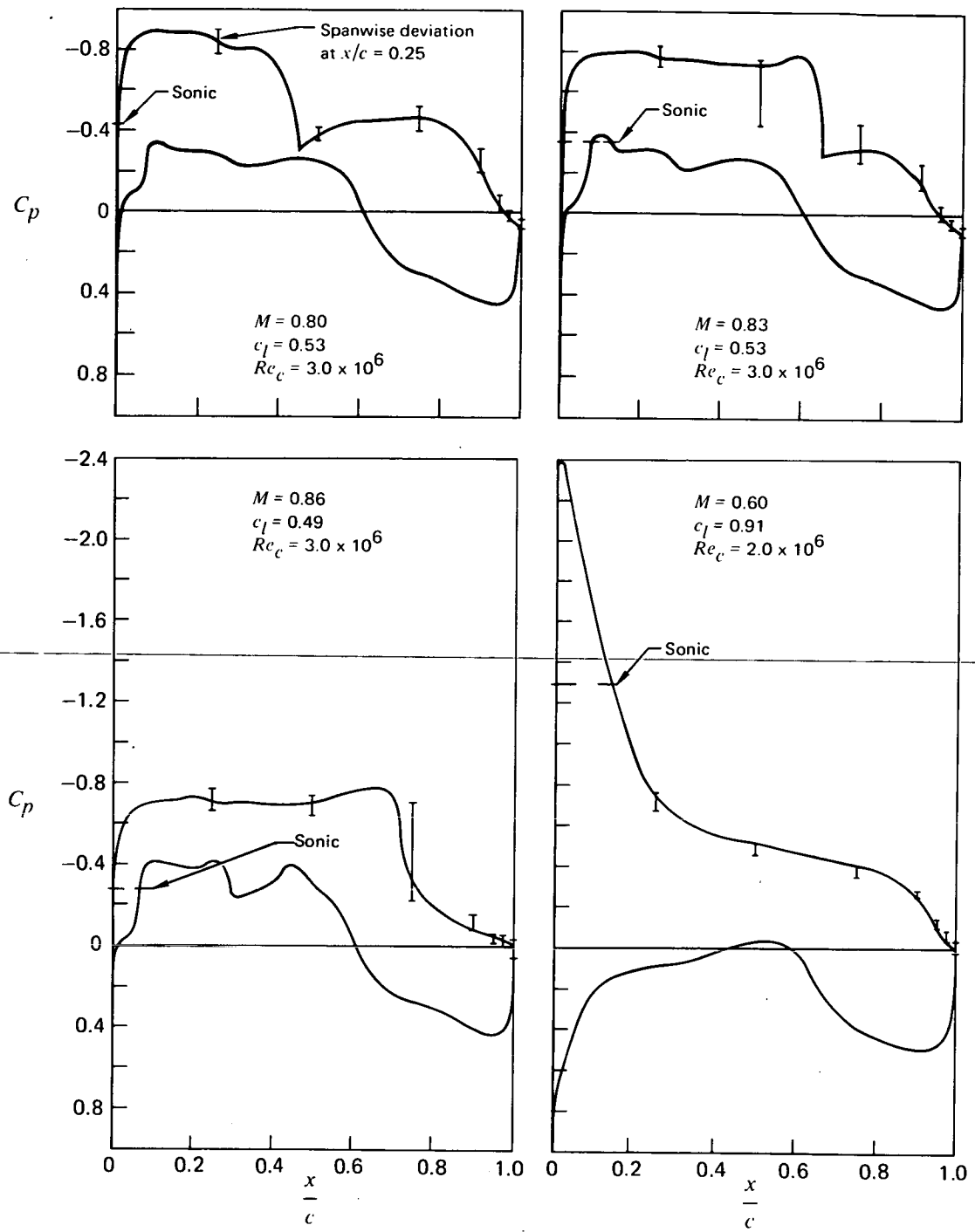

Figure 31.– Typical pressure distributions showing spanwise pressure deviation within the region $\pm y/c = 1.25$ at various x/c stations.

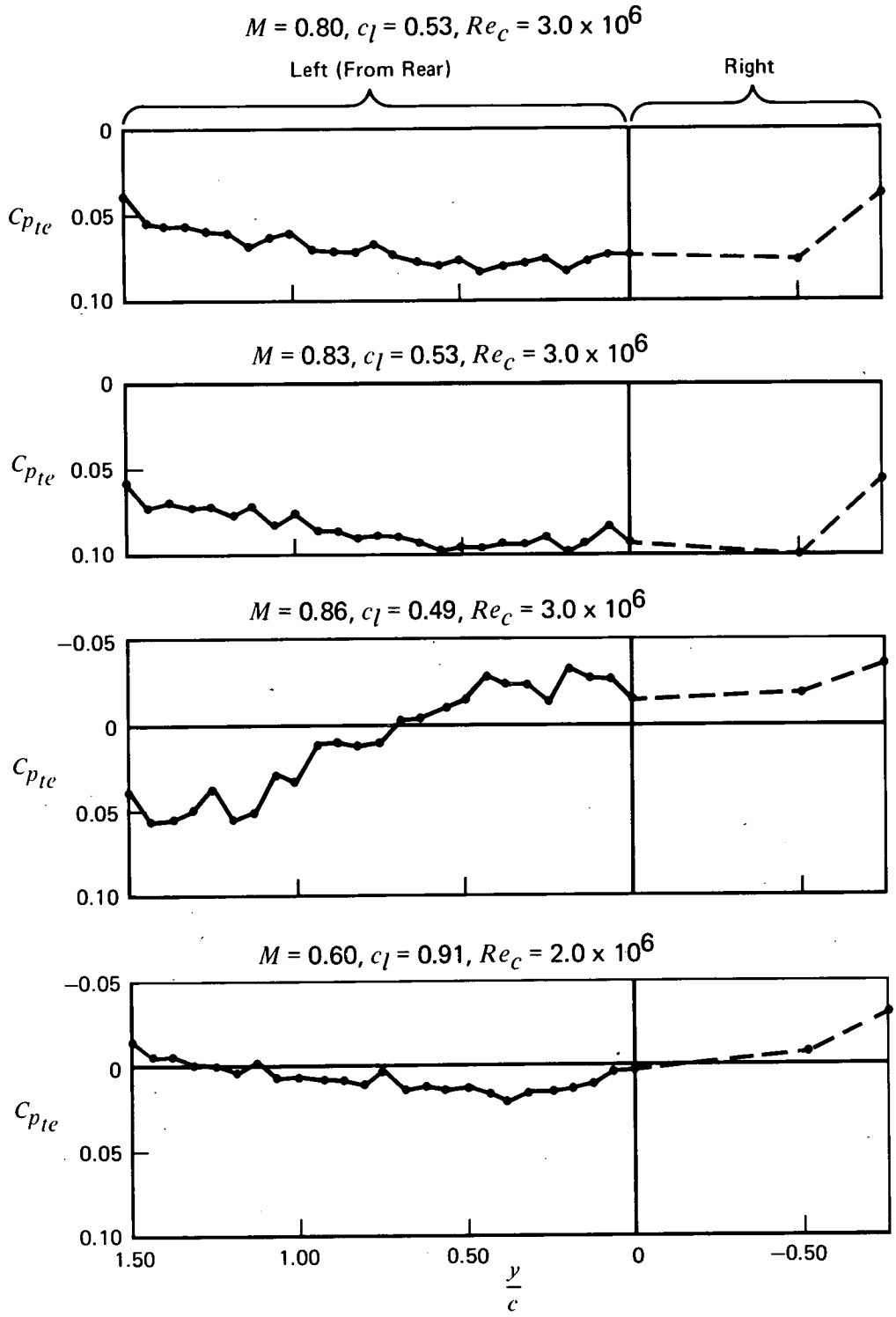

Figure 32.– Trailing edge pressure variation in the spanwise direction.

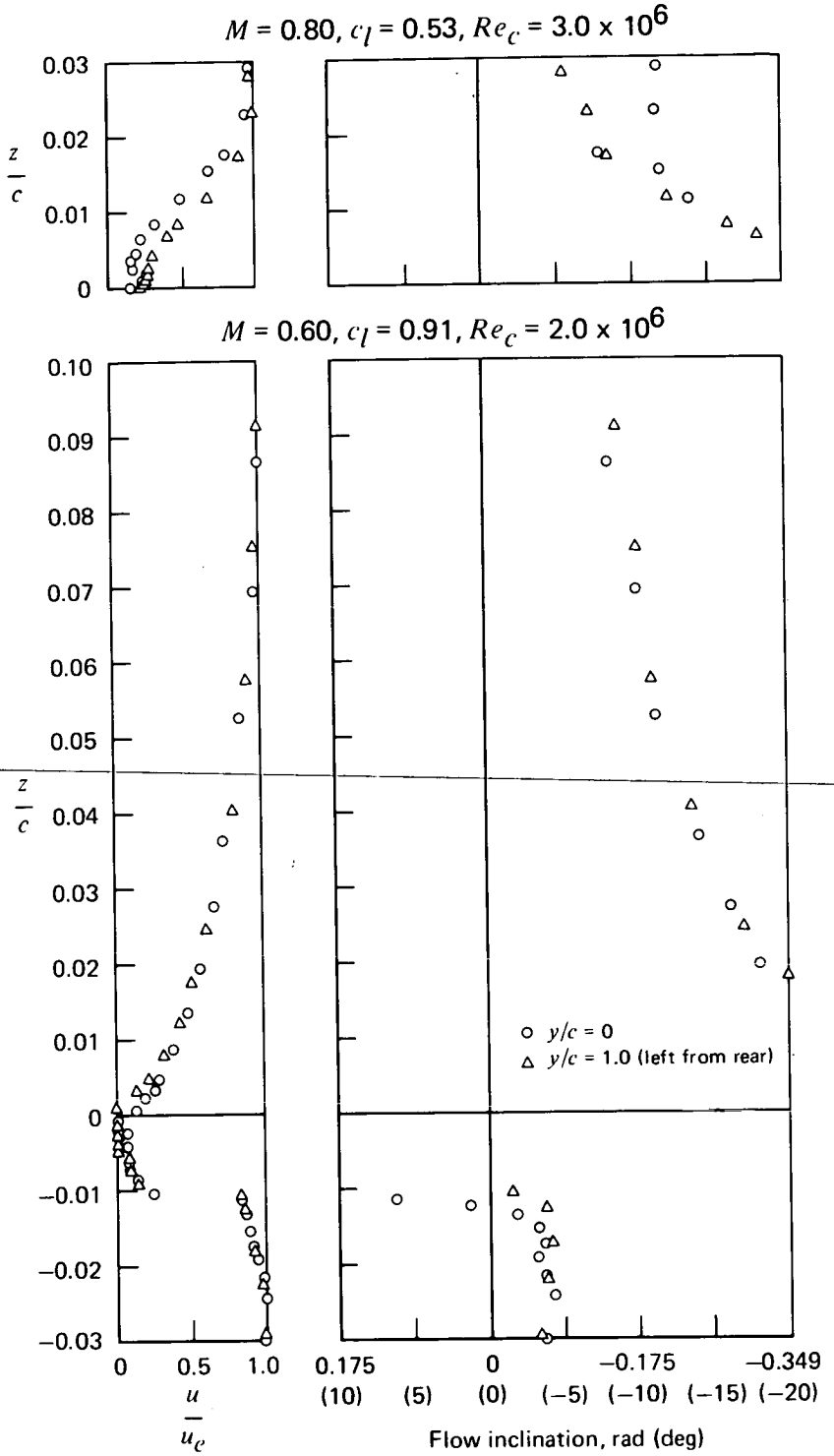

Figure 33.– Trailing edge speed and direction profiles at different spanwise stations.

NATIONAL AERONAUTICS AND SPACE ADMINISTRATION
WASHINGTON, D.C. 20546

OFFICIAL BUSINESS
PENALTY FOR PRIVATE USE $300

SPECIAL FOURTH-CLASS RATE
BOOK

POSTAGE AND FEES PAID
NATIONAL AERONAUTICS AND
SPACE ADMINISTRATION
451

U.S.MAIL

POSTMASTER: If Undeliverable (Section 158 Postal Manual) Do Not Return

"The aeronautical and space activities of the United States shall be conducted so as to contribute . . . to the expansion of human knowledge of phenomena in the atmosphere and space. The Administration shall provide for the widest practicable and appropriate dissemination of information concerning its activities and the results thereof."

—NATIONAL AERONAUTICS AND SPACE ACT OF 1958

NASA SCIENTIFIC AND TECHNICAL PUBLICATIONS

TECHNICAL REPORTS: Scientific and technical information considered important, complete, and a lasting contribution to existing knowledge.

TECHNICAL NOTES: Information less broad in scope but nevertheless of importance as a contribution to existing knowledge.

TECHNICAL MEMORANDUMS: Information receiving limited distribution because of preliminary data, security classification, or other reasons. Also includes conference proceedings with either limited or unlimited distribution.

CONTRACTOR REPORTS: Scientific and technical information generated under a NASA contract or grant and considered an important contribution to existing knowledge.

TECHNICAL TRANSLATIONS: Information published in a foreign language considered to merit NASA distribution in English.

SPECIAL PUBLICATIONS: Information derived from or of value to NASA activities. Publications include final reports of major projects, monographs, data compilations, handbooks, sourcebooks, and special bibliographies.

TECHNOLOGY UTILIZATION PUBLICATIONS: Information on technology used by NASA that may be of particular interest in commercial and other non-aerospace applications. Publications include Tech Briefs, Technology Utilization Reports and Technology Surveys.

Details on the availability of these publications may be obtained from:

SCIENTIFIC AND TECHNICAL INFORMATION OFFICE

NATIONAL AERONAUTICS AND SPACE ADMINISTRATION

Washington, D.C. 20546